



## Research paper

## Uranium-series isotopes as tracers of physical and chemical weathering in glacial sediments from Taylor Valley, Antarctica

Graham Harper Edwards <sup>a,\*</sup>, Gavin G. Piccione <sup>b</sup>, Terrence Blackburn <sup>c</sup>, Slawek Tulaczyk <sup>c</sup><sup>a</sup> Department of Earth & Environmental Geosciences, Trinity University, San Antonio, TX 78212, USA<sup>b</sup> Department of Earth, Environmental, and Planetary Sciences, Brown University, Providence, RI 02912, USA<sup>c</sup> Department of Earth and Planetary Sciences, University of California Santa Cruz, Santa Cruz, CA 95064, USA

## ARTICLE INFO

Communicated by Christian France-Lanord

Dataset link: <https://github.com/grahamedwards/CommWeath.jl>, <https://doi.org/10.15784/601806>

## Keywords:

Uranium-series geochemistry  
 Chemical weathering  
 Comminution  
 McMurdo Dry Valleys  
 Antarctica  
 Glacial erosion

## ABSTRACT

The McMurdo Dry Valleys of Antarctica formed by extensive glacial erosion, yet currently exhibit hyperarid polar conditions canonically associated with limited chemical and physical weathering. Efficient chemical weathering occurs when moisture is available, and polythermal subglacial conditions may accommodate ongoing mechanical weathering and valley incision. Taylor Valley, one of the MDV, hosts several Pleistocene glacial drift deposits that record prior expansions of Taylor Glacier and sediment redistribution, if not sediment production. We present U-series isotopes of fine-grained sediments from these drifts to assess the timescales of physical weathering and subsequent chemical alteration. The isotopes  $^{238}\text{U}$ ,  $^{234}\text{U}$ , and  $^{230}\text{Th}$  are sensitive to both chemical and physical fractionation processes in sedimentary systems, including the physical fractionation of daughter isotopes by energetic recoil following radioactive decay. By comparing U-series isotopic measurements with models of U-series response to chemical weathering and physical fractionation processes, we show that Pleistocene drift sediments record histories of significant chemical alteration. However, fine-grained sediments entrained in the basal ice of Taylor Glacier record only minor chemical alteration and U-series fractionation, indicating comparatively recent sediment comminution and active incision of upper Taylor Valley by Taylor Glacier over the Pleistocene. In addition, the results of this study emphasize the utility of U-series isotopes as tracers of chemical and physical weathering in sedimentary and pedogenic systems, with particular sensitivity to radionuclide implantation by  $\alpha$ -recoil from high-U authigenic phases into lower-U detrital phases. This process has occurred extensively in > 200 ka drifts but to a lesser degree in younger deposits. U-series  $\alpha$ -recoil implantation is an important physicochemical process with chronometric implications in other hyperarid and saline sedimentary systems, including analogous Martian environments.

## 1. Introduction

The Antarctic McMurdo Dry Valleys (MDV) are an extreme environment where hyperarid, polar conditions predict limited physical and chemical weathering processes that are seemingly at odds with other evidence for remarkably active weathering (Bockheim, 1997; Campbell and Claridge, 1981; Hallet et al., 1996; Lyons et al., 2021; Marra et al., 2017; Mager et al., 2007; Morgan et al., 2010). Low temperatures and moisture contents of MDV soils are thought to maintain extremely low chemical weathering rates that have preserved some soils for millions of years with minimal chemical alteration (Bockheim, 1997; Campbell and Claridge, 1981; Obryk et al., 2020). Similarly, physical erosion is limited both by low precipitation rates (<100 mm annually) that restrict glacial and fluvial erosion as well as by low annual air temperatures (<  $-14^\circ\text{C}$ , Doran et al., 2002) that limit erosion under permafrost and frozen subglacial conditions (Sugden and Denton, 2004).

In the modern climate, aeolian abrasion appears to be the predominant mechanism of physical erosion (Gillies et al., 2009), with contributions from thermal fatigue and endolithic biotic weathering (Hall and André, 2001; Hall et al., 2008). In contrast to these lines of evidence, vigorous aqueous chemical weathering occurs in the rare localities where liquid water does occur (Lyons et al., 2021; Marra et al., 2017), and deeply incised glacial valleys with thick sedimentary fills indicate periods of significant glacial erosion in the geologic past.

The erosive capacities of glaciers are closely linked to climate (Hallet et al., 1996). Warm and wet climates cause basal melting, which enhances ice sliding velocities and promotes efficient subglacial erosion and sediment transport. Cold and arid climates, such as those of the modern MDV, promote “cold-based” glaciers that remain frozen at their beds, resulting in relatively limited sediment production and

\* Corresponding author.

E-mail address: [gedward1@trinity.edu](mailto:gedward1@trinity.edu) (G.H. Edwards).

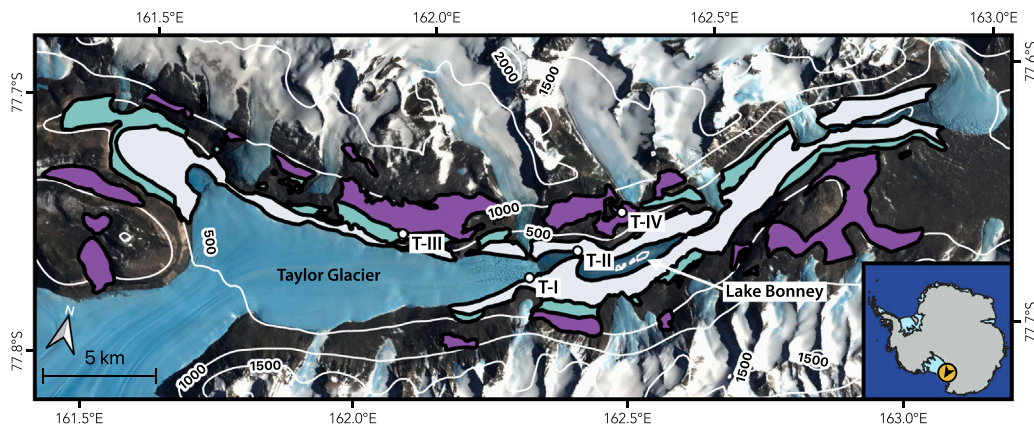


**Fig. 1.** Map of Taylor Valley, Antarctica and glacial drift deposits. Colors code the drift units as described by Bockheim et al. (2008), where T-IV and T-III respectively correspond to their Taylor-IVb and Taylor-III, IVa units. White points identify sample sites from this study, labeled with the corresponding drift unit. Inset: The continental location of Taylor Valley, Antarctica (yellow dot) with arrow orientation corresponding to North arrow in primary map. Prepared with Quantarctica (Matsuoka et al., 2021).

transport (Cuffey et al., 2000). To reconcile the glacially erosive history of the MDVs with their contemporary climate, models of MDV evolution invoke post-Paleocene (<55 Ma) climates that facilitated warm-based glacial conditions and active denudation until ~15 Ma (Denton et al., 1993; Sugden and Denton, 2004), after which transition to a hyperarid polar climate induced widespread cold-based conditions among MDV glaciers. Under this scenario, contemporary MDV glaciers only rearrange pre-Pliocene glacial deposits by cold-based processes with relatively restricted production and transport of new glacial sediments.

The exclusively cold-based model of MDV glaciers, however, is inconsistent with observations of Taylor Valley, where several lines of evidence imply at least partly wet-based, or polythermal, conditions beneath Taylor Glacier, an outlet of the East Antarctic Ice Sheet (EAIS; Fig. 1). Extensive englacial debris in Taylor Glacier imply melt-freeze processes of sediment entrainment (e.g. Mager et al., 2007), and ice penetrating radar indicates a high reflectivity zone of liquid water in an overdeepening beneath Lower Taylor Glacier (Hubbard et al., 2004). Despite predicted basal temperatures of  $\leq -7^{\circ}\text{C}$  at this location, high salinities may facilitate subsolidus liquid conditions, a scenario supported by the presence of Blood Falls—a subglacially fed hypersaline brine seep at the glacier's terminus (e.g. Badgeley et al., 2017). Such polythermal basal conditions could support efficient bedrock erosion and would account for the extensive Pleistocene drift sheets deposited by Taylor Glacier (Section 1.1). To further explore and resolve the conflicting evidence of both active and restricted weathering, we use U-series isotopes to interrogate the combined physical and chemical weathering histories of glacial sediments from Taylor Valley.

### 1.1. Modern setting & depositional history of Taylor Valley

Taylor Glacier flows from the Taylor Dome of the EAIS into upper Taylor Valley, terminating in the proglacial Lake Bonney (Fig. 1). The Asgard Range and Kukri Hills, which respectively border the valley to the North and South, host several alpine glaciers that flow into Taylor Valley (Fig. 1). In upper (western) Taylor Valley, Taylor Glacier sits atop Beacon Supergroup sedimentary rocks (primarily sandstones), and sills of Jurassic Ferrar dolerite and Quaternary mafic volcanics crop out at higher elevations (e.g. Hall et al., 2000). Taylor Glacier and the nearby alpine glaciers are currently at their maximum Holocene extents but no longer advancing (Denton et al., 1989; Hall et al., 2000; Fountain et al., 2006). At least four glacial drift sheets record prior Quaternary advances of Taylor Glacier (Denton et al., 1970), and Bockheim et al. (2008) summarized the distribution of these drifts, as shown in Fig. 1. The most ancient drift deposits are Taylor-IVb and the youngest are Taylor-I, which reflects the contemporary advancement of Taylor Glacier. For brevity, we adapt the nomenclature of Bockheim et al.

(2008) such that we use Taylor-III to describe the combined Taylor-III/Taylor-IVa grouping and Taylor-IV to describe the older Taylor-IVb unit.

Multiple geochronometric techniques constrain the depositional ages of the Taylor drift sheets. Taylor-IV drifts reflect the earliest recorded Taylor Glacier advance at  $\leq 2.7$  Ma based on  $^{40}\text{Ar}$ - $^{39}\text{Ar}$  ages of underlying volcanics (Wilch et al., 1993). The minimum age of Taylor-IV advance is constrained by cosmogenic  $^{10}\text{Be}$  dates from correlated moraines in nearby Arena Valley that require moraine emplacement before 1.5 Ma (Brook et al., 1993). Thus, Taylor-IV represents an ancient advance (or series of advances) of Taylor Glacier between 2.7 and 1.5 Ma, during which the ice margin reached elevations  $> 800$  m above the contemporary valley floor. The depositional ages of the younger Taylor-II and -III drifts are constrained by both cosmogenic exposure ages from Arena Valley moraines (Brook et al., 1993) and U-Th ages of lacustrine carbonates (Higgins et al., 2000; Hendy et al., 1979). The lacustrine carbonate formed when the Ross Ice Shelf dammed Taylor Valley during West Antarctic Ice Sheet expansion, forming a paleolake that flooded elevations up to ~300 m (above sea level, a.s.l.) in western Taylor Valley (Hall et al., 2000; Toner et al., 2013), which coincided with periods of reduced Taylor Glacier and EAIS extent (Higgins et al., 2000). In contrast, the cosmogenic exposure ages record boulder emplacement during Taylor Glacier expansion. Despite minor inconsistencies, these chronologies indicate deposition of Taylor-III between 450–250 ka and Taylor-II after 70 ka (Fig. 2).

The combined Taylor drift chronologies indicate a correlation between drift depositional age and contemporary elevation (Fig. 2). While this relationship is typical of glacial systems, it has important implications for the ice volume and erosional histories of Taylor Glacier. Under the canonical model of near-nil Plio-Pleistocene MDV glacial erosion rates, the drift age-elevation relationship reflects a decreasing trend in Taylor Glacier ice volumes during periods of EAIS expansion over the course of the Pleistocene. An alternative endmember model invokes Pleistocene incision by Taylor Glacier, whereby the polythermal subglacial conditions of Taylor Glacier accommodated significant erosion of the valley floor over the course of the Pleistocene (Fig. 2). While permitting variability in ice volumes, this model relates the age-elevation relationship of Taylor drifts to more consistent high-stand ice volumes and a gradually deepening valley floor. Although the known timescales of drift emplacement do not offer the ability to resolve these two plausible scenarios, we use the radiometric properties of the U-series system in fine-particles to discern whether the fine sediments that comprise Taylor drifts record ancient ( $> 1.5$  Ma) or recent ( $< 500$  ka) incision.

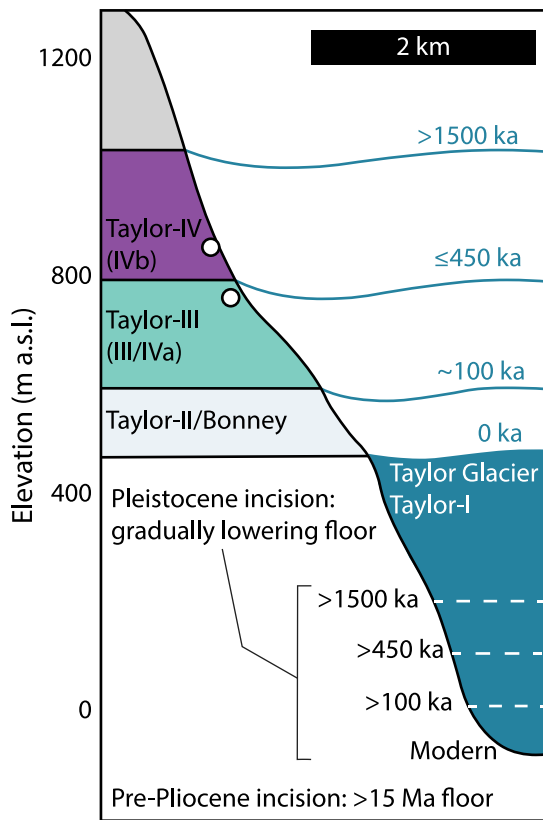


**Fig. 2.** Generalized cross-section of upper Taylor Valley illustrating the depositional history of Taylor drift sheets and endmember erosional histories described in the text. Blue curves identify the age and elevation of prior ice highstands constrained by previous chronological work. Under the pre-Pliocene incision model, negligible subglacial mechanical weathering since > 15 Ma has preserved the modern valley floor at the same elevation throughout the Pleistocene. Under the Pleistocene incision model, ongoing subglacial mechanical weathering has accommodated gradual valley incision up to the present. Circles demonstrate the elevations of Taylor-III (746 m) and Taylor-IV (878 m) drift samples. Taylor-I and Taylor-II sampling elevations (109 m and 113 m, respectively) are not included since these correspond to down-valley locations of thinned or terminated ice.

### 1.2. The effects of physical and chemical weathering on U-series systematics of fine particles

The weathering of fine particles traditionally includes two components: a physical component of mechanical comminution from larger particles to finer particles and a chemical component of mineral dissolution and precipitation. Subglacial comminution processes tend to converge on sand-to-silt-sized particles (2000–5  $\mu\text{m}$  diameters) that resist further physical comminution to smaller sizes (Haldorsen, 1981). Hence, in the context of this study we expect that physical weathering happens only early on in the history of most glaciogenic sand-to-silt-sized sediments, after which chemical weathering takes on an enhanced role as primary detrital material is dissolved and replaced by authigenic mineral phases.

In closed geologic systems over >1.5 Ma durations, the ingrowth and outgrowth of intermediate daughter products cause the relative amounts of isotopes in the  $^{238}\text{U}$  decay series to converge on equilibrium values, nominally secular equilibrium (SE), which is represented by parent-daughter activity ratios of unity, e.g.  $(^{234}\text{U}/^{238}\text{U})=1$ . After any perturbation that drives the system out of SE, a parent-daughter ratio converges within ~1% of SE after 6 half-lives ( $t_{1/2}$ ) of the short-lived isotope. In the present study, we consider the U-series isotopes  $^{238}\text{U}$ ,  $^{234}\text{U}$ , and  $^{230}\text{Th}$ . Although  $^{238}\text{U}$  decays to  $^{234}\text{U}$  via the short-lived isotopes  $^{234}\text{Th}$  ( $t_{1/2} \sim 24$  days) and  $^{234}\text{Pa}$  ( $t_{1/2} \sim 1.2$  minutes),

their lifetimes are geologically negligible, and we treat  $^{238}\text{U}$  as decaying directly to  $^{234}\text{U}$ . The following sections consider how chemical and physical weathering processes affect the  $^{230}\text{Th}$ - $^{234}\text{U}$ - $^{238}\text{U}$  systematics of fine-grained particles derived from ancient bedrock in SE.

#### 1.2.1. The effects of physical weathering on the $^{238}\text{U}$ decay series

Following the reduction of material to silt-sized (<50  $\mu\text{m}$  diameter) particles, the U-series system progresses into disequilibrium from the physical fractionation of intermediate daughter products by energetic recoil of nuclides produced during radioactive  $\alpha$ -decay. Within mineral grains, as radionuclides (e.g.  $^{238}\text{U}$  and  $^{234}\text{U}$ ) undergo  $\alpha$ -decay, an  $\alpha$ -particle ( $^4\text{He}$  nucleus) is ejected from the parent nucleus and the newly produced radiogenic daughter nuclide recoils in the opposite direction through the surrounding crystalline matrix in response to the energetic  $\alpha$ -emission. In framework silicates (e.g. feldspars and quartz), this recoil distance is approximately ~35 nm, though it varies slightly among the different  $\alpha$ -decay products (Semkow, 1991). If the decay occurs near the surface of the mineral grain, the daughter nuclide may be ejected from the grain and lost from the mineral system (Fig. 3a). Thus, fine-grained particles (<50  $\mu\text{m}$  diameter) exhibit a measurable reduction in  $(^{234}\text{U}/^{238}\text{U})$  below SE due to  $\alpha$ -recoil loss of  $^{234}\text{U}$  after  $^{238}\text{U}$  decay (Ku, 1965; DePaolo et al., 2006). Although  $\alpha$ -recoil ejection of  $^{234}\text{U}$  also occurs in larger grains (Kigoshi, 1971), the disequilibrium only becomes detectable in grains with diameters <50  $\mu\text{m}$ , where the particles have a sufficiently high surface-area-to-volume ratio to incur  $^{234}\text{U}$  loss in amounts measurable by modern mass spectrometric methods (> 0.1%). After 1.5 Ma (six half-lives of  $^{234}\text{U}$ ) the  $(^{234}\text{U}/^{238}\text{U})$  reaches a new equilibrium controlled by the sediment grain size and surface morphology (Fig. 3b). Fine particles comminuted prior to 1.5 Ma maintain a low  $(^{234}\text{U}/^{238}\text{U})$  that reflects this antiquity. Prior authors (e.g. Lee et al., 2010; Cogez et al., 2018) have speculated that the same principles apply to subsequent intermediate daughter nuclides with shorter half-lives, such as  $^{230}\text{Th}$ , which would exhibit similar behavior to  $^{234}\text{U}$ , differing only in their convergence on slightly different equilibrium values (Fig. 3b). This time-dependent  $\alpha$ -recoil loss from freshly comminuted particles forms the theoretical foundation of U-series comminution dating (DePaolo et al., 2006).

The rate and degree of daughter nuclide depletion is dependent on a particle's physical properties, which dictate the proportion of decays that result in  $\alpha$ -recoil ejection. Two simple approaches summarize these properties with a fractional loss factor  $f_m$ , where  $m$  denotes the mass of the radiogenic nuclide, e.g. 234 for  $^{234}\text{U}$ . The first formulation, Eq. (1a) (after Semkow, 1991; DePaolo et al., 2006), calculates the fractional loss factor for a given radiogenic nuclide as a function of the effective recoil length ( $L_m$ ), the sediment specific surface area ( $S$ ), and the sediment density ( $\rho$ ). The second formulation, Eq. (1b) (after Lee et al., 2010), replaces the  $S$  term with grain size parameters (Eq. (1c), after Anbeek et al., 1994): diameter ( $d$ ), a dimensionless grain shape factor ( $K$ , after Cartwright, 1962), and a surface roughness factor ( $\lambda_r$ ):

$$f_m = (L_m \cdot S \cdot \rho)/4 \quad (1a)$$

$$f_m = (L_m \cdot K \cdot \lambda_r)/(4d) \quad (1b)$$

$$S = (\lambda_r \cdot K)/(\rho \cdot d) \quad (1c)$$

The  $f$  parameter for some model silicate grain may then be combined with standard U-series decay equations (e.g. Bateman, 1910), to model the grain's time-dependent radioisotopic evolution.

$$\frac{dN_{238}}{dt} = -\lambda_{238} N_{238} \quad (2a)$$

$$\frac{dN_{234}}{dt} = -\lambda_{234} N_{234} + (1 - f_{234})\lambda_{238} N_{238} \quad (2b)$$

$$\frac{dN_{230}}{dt} = -\lambda_{230} N_{230} + (1 - f_{230})\lambda_{234} N_{234} \quad (2c)$$

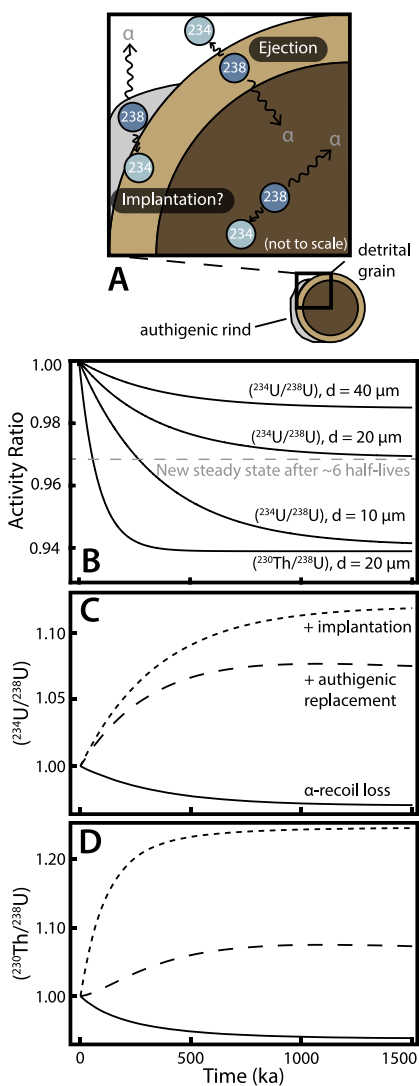


**Fig. 3.** (A) Diagram of  $\alpha$ -recoil processes that affect the U-series isotopic compositions of particles. For ancient particles in secular equilibrium,  $\alpha$ -recoil within the grain interior does not affect the particle's isotopic composition. Within  $\lesssim 40$  nm of the grain surface,  $\alpha$ -recoil ejection or implantation leads to isotopic disequilibrium in this zone that measurably affects the bulk-grain isotopic composition. (B) Simulated U-series isotope evolutions due to  $\alpha$ -recoil ejection in idealized silt-sized particles. Curves are labeled with modeled activity ratios and particle diameter ( $d$ ). Following comminution (time = 0 ka), activity ratios decrease at a rate controlled by grain morphology and the rate of radioactive decay, converging on a new grain-size-controlled equilibrium within six half-lives. (C,D) Modeled U-series isotope evolutions of a 20  $\mu\text{m}$  diameter detrital grain affected by: only  $\alpha$ -recoil loss (solid curves),  $\alpha$ -recoil loss and authigenic replacement of primary material (dashed), and  $\alpha$ -recoil loss and implantation from an adjacent high-U authigenic phase (dotted curves). Assumes authigenic phase  $(^{230}\text{Th}/^{238}\text{U}) = (^{234}\text{U}/^{238}\text{U}) = 3$ .

These equations may be solved numerically, assuming initial isotopic compositions, which for sediment freshly comminuted from an ancient bedrock source are expected to reflect SE,  $(^{234}\text{U}/^{238}\text{U}) = (^{230}\text{Th}/^{238}\text{U}) = 1$ . In this idealized scenario, the activity ratios for the various grain sizes decrease from unity to a new, grain-size defined equilibrium composition (Fig. 3c,d). With a well-constrained  $f_{^{234}\text{U}}$ , one may calculate a “comminution age” from the measured  $(^{234}\text{U}/^{238}\text{U})$ .

#### 1.2.2. Chemical weathering effects on the U-series system

Accurate and precise comminution dates have remained elusive because sedimentary systems are also characterized by chemical weathering and authigenic mineral forming processes that affect the U-series

system (e.g. Handley et al., 2013; Suresh et al., 2014; Martin et al., 2015; Menozzi et al., 2016). The most straightforward process of chemical weathering is dissolution of primary “detrital” material, which releases ions from the crystalline matrix of detrital minerals into the surrounding (typically aqueous) environment. Given the association of  $^{234}\text{U}$  with damaged zones in mineral lattices, this isotope is preferentially leached compared to its parent  $^{238}\text{U}$  (Andersen et al., 2009). In contrast, the typically lower solubility of Th predicts an excess of  $^{230}\text{Th}$  relative to  $^{234}\text{U}$  and  $^{238}\text{U}$  following chemical weathering (Chabaux et al., 2003; Suresh et al., 2013; Menozzi et al., 2016; Cogez et al., 2018). To account for simple chemical weathering by dissolution and leaching of primary detrital mineral, an additional weathering rate term  $k$  may be incorporated into Eq. (2) to capture the combined effects of silicate dissolution and  $\alpha$ -recoil ejection of U-series nuclides, following the equations of Chabaux et al. (2003), Dosseto and Schaller (2016), and Cogez et al. (2018):

$$\frac{dN_{^{238}\text{U}}}{dt} = -k_{^{238}\text{U}}N_{^{238}\text{U}} - \lambda_{^{238}\text{U}}N_{^{238}\text{U}} \quad (3a)$$

$$\frac{dN_{^{234}\text{U}}}{dt} = -k_{^{234}\text{U}}N_{^{234}\text{U}} - \lambda_{^{234}\text{U}}N_{^{234}\text{U}} + (1 - f_{^{234}\text{U}})\lambda_{^{238}\text{U}}N_{^{238}\text{U}} \quad (3b)$$

$$\frac{dN_{^{230}\text{Th}}}{dt} = -k_{^{230}\text{Th}}N_{^{230}\text{Th}} - \lambda_{^{230}\text{Th}}N_{^{230}\text{Th}} + (1 - f_{^{230}\text{Th}})\lambda_{^{234}\text{U}}N_{^{234}\text{U}} \quad (3c)$$

where the value of  $k$  varies from isotope to isotope based on how readily it is weathered (e.g.  $k_{^{234}\text{U}} > k_{^{238}\text{U}} > k_{^{230}\text{Th}}$ ).

However, chemical weathering is a bidirectional process, comprised of both dissolution of detrital phases and precipitation of authigenic phases. Generally, authigenic phases are precipitated from aqueous solution and incorporate cations from the aqueous and sedimentary environment, including U and Th. Since surface waters are typically characterized by supra-SE ( $^{234}\text{U}/^{238}\text{U}$ ) compositions (Andersen et al., 2009, and references therein), authigenic phases tend to increase the ( $^{234}\text{U}/^{238}\text{U}$ ) of sediments (Martin et al., 2015). Martin et al. (2015) showed that sequential chemical extractions that dissolve specific authigenic phases such as oxide species, carbonates, and organic compounds each effectively remove U and change the ( $^{234}\text{U}/^{238}\text{U}$ ) of the insoluble residues. In addition, non-silicate authigenic phases are complimented by authigenic silicate minerals, including “clay” minerals. While this term is also used to describe particle sizes  $<4 \mu\text{m}$ , we will use the term exclusively in a mineralogical sense to describe authigenic clay minerals. Like their non-silicate counterparts, authigenic clay minerals form by aqueous precipitation following dissolution of silicate minerals and therefore reflect  $(^{234}\text{U}/^{238}\text{U}) > 1$  parent-water compositions. Insoluble Th will preferentially leave the water column by adsorbing onto particle surfaces or partitioning into authigenic phases, resulting in elevated ( $^{230}\text{Th}/^{238}\text{U}$ ). Indeed, Menozzi et al. (2016) have shown that silicate clay minerals can persist through leaching techniques and impart elevated ( $^{234}\text{U}/^{238}\text{U}$ ) and ( $^{230}\text{Th}/^{238}\text{U}$ ). The degree of excess above SE scales with the U and Th content of authigenic phases as well as the duration and extent of weathering (Fig. 3C,D).

Authigenic phases may also affect the U-series systems of adjacent detrital grains by implanting  $^{234}\text{U}$  and  $^{230}\text{Th}$  during  $\alpha$ -recoil across the interface between the authigenic and detrital phases (Fig. 3A). As long as the adjacent authigenic phase is more uraniferous than the detrital phase, there will be a net positive flux of daughter isotopes to the detrital phase across the interface, enriching the detrital grain in  $^{234}\text{U}$  and  $^{230}\text{Th}$  (Fig. 3C,D). If this authigenic phase is soluble in any pretreatments or chemical extractions prior to final sediment digestion, the  $^{234}\text{U}$ - and  $^{230}\text{Th}$ -depleted authigenic phase is lost in these steps, leaving only the insoluble and  $^{234}\text{U}$ ,  $^{230}\text{Th}$ -enriched detrital phase. The longer this contact between the high-U soluble phase and lower-U insoluble phase persists, the higher the ( $^{234}\text{U}/^{238}\text{U}$ ) and ( $^{230}\text{Th}/^{238}\text{U}$ ) in the insoluble phase, until a new long-term equilibrium is reached (Fig. 3C,D). The process of  $\alpha$ -recoil implantation has been observed between the high- and low-U phases of igneous rocks (Tanaka et al., 2015) and primary silicate phases of igneous regolith (Menozzi et al., 2016), but its role in sedimentary systems has remained speculative (Lee et al., 2010; Plater et al., 1992).

### 1.3. Exploring the timescales of physical and chemical weathering in Taylor Valley with U-series isotopes

This study expands on the aforementioned mathematical and theoretical models of sedimentary U-series geochemistry to predict the U-series evolutions of sediments subjected to  $\alpha$ -recoil loss, chemical dissolution, authigenic mineral formation, and  $\alpha$ -recoil implantation. We use these models to interpret the  $^{230}\text{Th}$ - $^{234}\text{U}$ - $^{238}\text{U}$  systems of proglacial and englacial sediments from Taylor Valley in the context of chemical and physical weathering processes. Within this framework, we explore the potential of U-series records of both physical fractionation and chemical alteration to discern the timescales of fine-particle production in Taylor Valley.

The physical weathering of Taylor Valley has been dominated by glacial wear processes. Beneath glaciers, mechanical crushing and abrasion readily comminute coarse material to sand- and silt-sized particles, respectively, that resist further comminution (Haldorsen, 1981). The chemical weathering environment of Taylor Valley and the greater MDV system is less straightforward and highly dependent on the availability of water. Outside of lakes and the hyporheic zones of streams, chemical weathering in the MDV occurs very slowly, limited largely to the oxidation of ferrous minerals and minor production of authigenic clays (Campbell and Claridge, 1981). Older soils at higher elevations in Taylor Valley are indurated with abundant soluble salts that refute any recent aqueous chemical alteration (Bockheim, 2002). However, at lower elevations of Taylor Valley, most salt accumulations reflect the evaporative residues of prior paleolake highstands, such as when the lake levels rose to >300 m elevations in western Taylor Valley during Marine Isotope Stage 2 (Toner et al., 2013; Hall et al., 2000). Contemporarily, areas of liquid water saturation facilitated by high salinities reflect far more active chemical weathering, evidenced by an increase in clay fraction and sediment surface area (Campbell and Claridge, 1981; Marra et al., 2017). Indeed, chemical alteration rates in saturated zones of Taylor Valley sediment indicate more efficient chemical weathering than previously thought for the MDVs (Lyons et al., 2021).

Given the heterogeneous nature of chemical weathering in Taylor Valley, we take especial care to simplify our study of Taylor Valley sediment by limiting the many mechanisms of mechanical weathering. For each drift sample, we focus on two mineralogical groups: framework silicates (quartz and feldspars) and clays. Quartz and feldspar are generally more resilient to chemical weathering than phyllosilicates and mafic phases and offer the added benefit of well-constrained and relatively consistent  $\alpha$ -recoil lengths (Sun and Semkow, 1998). To further ensure the specificity of our study, we use chemical cleaning procedures that remove known non-silicate authigenic phases. We concurrently explore the U-series behavior of clay minerals to explore how these authigenic silicates are related to detrital materials. Finally, by examining the three-isotope  $^{230}\text{Th}$ - $^{234}\text{U}$ - $^{238}\text{U}$  system across a range of “silt” particle sizes (10–20, 20–38, and 38–45  $\mu\text{m}$ ), we gain the added insight of the integrated chemical and physical processes that fractionate  $^{230}\text{Th}$  in addition to those physical processes involved in the fractionation of U isotopes. Within this framework, we test the hypothesis that the U-series systems of silts in Taylor Valley record the timeframes of physical comminution and authigenic chemical processes. We identify and explore the relevant weathering processes affecting U-series isotopes and use these to resolve whether efficient subglacial comminution beneath Taylor Glacier ceased after warmer Pliocene conditions or has continued throughout the Pleistocene.

## 2. Materials and methods

### 2.1. Field methods and sample handling procedures

We collected drift sediment and debris-rich glacial ice from Taylor Valley during the austral spring of 2017 (Fig. 1). We sampled drift

sediments from pits dug to ~50 cm depth below the surface, taking care to sample beneath any apparent sedimentary fabrics and indurated salt crusts to ensure the samples represented original till deposits that had minimally interacted with surface snowmelt or running water. Debris-rich ice samples were chipped out of Taylor Glacier using a steel ice-chisel, targeting bands of sediment-laden basal ice. Ice samples were stored in plastic bags at -20°C before melting under laboratory conditions.

### 2.2. Laboratory and analytical methods

#### 2.2.1. Grain-size separation and mineralogical purification

Our study targeted 10–45 and 75–125  $\mu\text{m}$  diameter sediments of quartz-feldspar and clay mineralogy. We first separated silt-sized grains from bulk sediment by dry-sieving to grain diameters of <38  $\mu\text{m}$ , 38–45  $\mu\text{m}$ , and 75–125  $\mu\text{m}$  (only the 90–125  $\mu\text{m}$  fraction was recovered for sample Taylor-III). The <10  $\mu\text{m}$  component was removed from the <38  $\mu\text{m}$  aliquot by wet sieving. The 10–38  $\mu\text{m}$  separates were dry-sieved to 10–20  $\mu\text{m}$  and 20–38  $\mu\text{m}$  diameter ranges with a Gilsonic UltraSiever sonic sieving device.

For each size range, we removed clay mineral phases with a Stokes settling hydraulic separation. We preferentially removed clay mineral phases by vigorously swirling sediments in water and allowing grains to settle for  $\geq$ 10 min before pouring off suspended material and repeating the procedure  $\geq$ 3 times. We recovered both the clay-rich components decanted with the supernatant (slow hydraulic settling), as well as the clay-poor “detrital” component (rapid hydraulic settling). The clay-rich components were leached without further purifications, whereas the settled, detrital components were further purified with magnetic and density separations.

We removed Fe-bearing phases with a Frantz magnetic separator (0.6 A magnetic field and 17° slope). We removed phosphate and zircon mineral phases by density separation in 2.85 g  $\text{cm}^{-3}$  LST heavy liquid. Purified quartz-feldspar mineralogies were recovered from the buoyant component. For samples Taylor-I, Taylor-II, and Taylor-IV, density separations lasted for 1 h of settling time, whereas density separations for Taylor-III lasted for 10 min aided by low-speed centrifugation. These procedures yielded purified quartz-feldspar separates of three discrete “silt” grain size ranges (10–20  $\mu\text{m}$ , 20–38  $\mu\text{m}$ , and 38–45  $\mu\text{m}$ ) as well as a “sand” grain size range (75–125  $\mu\text{m}$ ). Mineralogical purity was confirmed by visual inspection under a binocular picking microscope.

For the englacial sediments of the Taylor-I sample, sediments were frozen within ice. Prior to mineralogical separations, we melted the ice in the presence of <0.05 M Ethylenediaminetetraacetic acid (EDTA) buffered with ammonia to pH > 10 before sediments were dried and underwent mineralogic purification. This treatment had no discernible effect on U-series isotopes, as verified by an aliquot of Taylor-IV that was subjected to the same EDTA treatment (see sample TV-IV-R3L-5, Appendix Table A.1).

#### 2.2.2. Sequential chemical extraction or “leaching” methods

Prior to digestion and isotope dilution, some samples were chemically cleaned with a sequential extraction method (hereafter “leaching” for brevity) using reagents that preferentially dissolve specific secondary mineral phases, while leaving silicate phases unperturbed. Leaching methods were modified from sequential extraction protocols that target various authigenic phases (Tessier et al., 1979; Poulton and Canfield, 2005; Lee et al., 2010), and each step is briefly outlined in Table 1. For each leach step, samples reacted with 50 mL of reagent.

Leaching procedures were performed in PFA centrifuge tubes cleaned in a > 50°C 7M  $\text{HNO}_3$  bath for > 12 hours. All reactions were continuously agitated throughout the prescribed duration: room-temperature reactions with a vertical rotation shaker and reactions held at 90°C with an orbital shaker dry-bath. Following each step, the samples were centrifuged and the leachate decanted. The residue was rinsed and briefly agitated with 50 mL of ultra-pure water, centrifuged,

**Table 1**  
Sequential extraction to remove soluble non-silicate authigenic phases.

Targeted phase	Procedure
Amorphous Fe oxides	0.2 M ammonium oxalate + 0.2 M oxalic acid agitated at room temperature for $\geq 8$ h
Crystalline Fe oxides	0.2 M ammonium oxalate + 0.2 M oxalic acid + 114 mM ascorbic acid agitated at 90°C for $\geq 8$ h
Mn oxides	25% acetic acid + 0.04 M hydroxylammonium chloride agitated at 90°C for $\geq 8$ h
Organic matter	30% H <sub>2</sub> O <sub>2</sub> adjusted to pH 2 with 0.02 M HNO <sub>3</sub> agitated at 90°C for $\geq 6$ h (additional 10 ml aliquots of reagent added at hours 4 and 5)
Carbonates	0.25 M HCl agitated at room temperature > 4 h

and the rinse decanted. This rinsing procedure was repeated three times before advancing to the next leaching step. For all leached fractions reported herein, the five-step procedure was repeated for a total of either three or five iterations.

#### 2.2.3. Isotope dilution, digestion, elemental purification, and mass spectrometry

The following methods were performed in a class 1000 clean lab using triple-distilled or ultra-pure trace metal grade reagents and ultra-pure water (deionized to 18 megohms-cm). All beakers and digestion vessels were acid-cleaned. PFA beakers refluxed a 14M HF – 3M HNO<sub>3</sub> solution for  $\geq 24$  h followed by 6M HCl for  $\geq 24$  h at 110°C. Microwave digestion vessels underwent full digestion cycles (described below) with cleaning acid, followed by refluxing 6M HCl.

Prior to digestion, sediment fractions were triple-rinsed with 50 ml of ultra-pure water. After rinsing, the sediment was dried, massed, and added to a dissolution vessel and spiked with an in-house-calibrated <sup>229</sup>Th-<sup>236</sup>U tracer prior to dissolution. Typical fraction masses were  $\sim 250$  mg for leached sediment and 50–100 mg for unleached sediment. Samples were digested one of two ways: (1.) in a mixture of 6 ml concentrated HF and 200  $\mu$ l concentrated HNO<sub>3</sub> for 15 min at 150°C with an Anton Paar MultiWave Go microwave digestion system, or (2.) in a mixture of 5 ml concentrated HF and 1 ml concentrated HNO<sub>3</sub> in a covered 15 ml PFA beaker on a 110°C hotplate for 48 h. No systematic difference in isotopic composition or blank were observed between these two methods. Microwave-digested solutions were transferred to 15 ml PFA beakers following dissolution.

Digested solutions were evaporated to dryness and redissolved in 5 ml 3M HCl with 250  $\mu$ l 2.5M HCl saturated with H<sub>3</sub>BO<sub>3</sub> to eliminate metal-fluoride complexes. For this and all subsequent rehydration steps, we refluxed the samples for several hours to allow complete dissolution and chemical equilibration. We evaporated the solutions and rehydrated them with 5 ml 1M HCl. This process was repeated twice to evaporate residual H<sub>3</sub>BO<sub>3</sub>. To convert samples to nitrate salts for column chemistry, samples were twice evaporated and rehydrated with 5 ml of 7M HNO<sub>3</sub>. Samples were finally evaporated and rehydrated in 3 ml 7M HNO<sub>3</sub> for introduction to column chemistry.

Th and U were purified from bulk solution with a two-column process. Primary separations were performed on a 2 ml resin bed of AG 1-X8 (200–400  $\mu$ m mesh) resin. Samples were loaded onto cleaned and preconditioned resin in 3 ml of 7M HNO<sub>3</sub>. We eluted matrix elements with 3 ml 7M HNO<sub>3</sub> followed by 0.5 ml 6M HCl. Then, Th was eluted in 4 ml 6M HCl, followed by U in 4 ml water. The eluted loading acid and 7M HNO<sub>3</sub> washes contained up to 50% of the total Th, so these elutions were reserved and reloaded onto the column (6 ml total) and washed with 3 ml 7M HNO<sub>3</sub> followed by 0.5 ml 6M HCl. The Th was eluted in 4 ml 6M HCl and combined with the initial Th elution. U and Th elutions were then evaporated, converted to nitrate salts by refluxing in 0.5 ml concentrated HNO<sub>3</sub>, and then dried and rehydrated in 1 ml 7M HNO<sub>3</sub> for introduction to U and Th clean-up columns, following the methods of [Blackburn et al. \(2020\)](#). Purified U and Th elutions were evaporated to dryness and rehydrated in 250  $\mu$ l 30% H<sub>2</sub>O<sub>2</sub> and refluxed

for  $\geq 1$  h to eliminate any organic materials inherited from the resin. Finally, samples were evaporated just to dryness with trace H<sub>3</sub>PO<sub>4</sub> for mass spectrometric analysis.

Isotopic compositions of U and Th were measured on the IsotopX X62 Phoenix Thermal Ionization Mass Spectrometer in the UC Santa Cruz W.M. Keck Isotope Laboratory. We loaded U onto Re ribbon (99.99% purity) with a Si gel-0.035M H<sub>3</sub>PO<sub>4</sub> activator and measured isotopes as oxides using a dynamic Faraday-Daly method ([Blackburn et al. 2020](#)). Th was loaded with 1  $\mu$ l 5% HNO<sub>3</sub> onto Re ribbon coated with graphite. Isotopes of Th were measured as a metal using a peak hopping method. Isotopes <sup>230</sup>Th and <sup>229</sup>Th were measured on the Daly-photomultiplier complex, while the high abundance of <sup>232</sup>Th required measurement by Faraday cup. A <sup>230</sup>Th-<sup>232</sup>Th Faraday-Daly correction was calibrated from repeated measurements (n=30) of the standard UCSC ThA and the accepted composition of [Rubin \(2001\)](#). However, Faraday-Daly Th ratios (i.e. <sup>232</sup>Th/<sup>229</sup>Th and <sup>230</sup>Th/<sup>232</sup>Th) were sometimes unstable due to Daly-Photomultiplier gain drift on the timescales of individual measurements. As a result, measurements of <sup>232</sup>Th are not consistently reproducible (Appendix Fig. A.1), and are therefore only semi-quantitative. Measurements of all other U and Th isotopes, however, are fully quantitative.

We corrected all measurements for instrument fractionation and tracer and blank contributions with an algorithm that fully propagates uncertainties. Concurrent total procedural blanks were measured throughout the study, confirming U and Th blanks reliably  $\ll 1$  ng, with typical blank amounts of both U and Th of  $\sim 100$  pg. We calculated model blank compositions from long-term means of total procedural blanks. Blank corrections did not significantly affect isotope ratios. The accuracy and reproducibility of <sup>230</sup>Th-<sup>234</sup>U-<sup>238</sup>U isotope measurements were verified by concurrent digestion, chemical purification, and measurement of USGS rock standard BCR-2 (Appendix Fig. A.1).

#### 2.3. Major element compositions and chemical index of alteration

In addition to U-Th isotopes, we measured the major element compositions of several leached detrital (rapid hydraulic settling) aliquots. We digested  $\sim 10$  mg fractions using a scaled-down version of the digestion methods for isotopic analyses described above. Dissolved fractions were converted to nitrate salts, diluted, and atomic abundances measured via inductively-coupled plasma optical emission spectrometry (ICP-OES) at the University of California Santa Cruz Plasma Analytical Laboratory. Unknown major element abundances were calculated relative to a standard of concurrently prepared dissolution of BCR-2. We validated the accuracy of these measurements by reproducing accepted major element compositions of the AThO rock standard. We use the accepted values from the GeoReM database for the major element compositions of both standards ([Jochum et al., 2005](#)).

In addition to reporting major element compositions, we calculate and report two forms of the chemical index of alteration (CIA). The CIA is calculated after [Nesbitt and Young \(1982\)](#), using oxide weight percentages:  $CIA = 100 \times [Al_2O_3 / (Al_2O_3 + CaO^* + Na_2O + K_2O)]$ , where CaO\* describes the weight percent CaO contained within the

**Table 2**  
Selected values for parameters used to calculate  $f_m$  values with Eq. (1).

Parameter	Description	Value	Reference	Notes
$L_{234}$	$^{234}\text{Th}$ recoil distance	34 nm	Sun and Semkow (1998)	Mean simulated value.
$L_{230}$	$^{230}\text{Th}$ recoil distance	37 nm	Sun and Semkow (1998)	Mean simulated value.
$K$	Grain shape factor	10	Cartwright (1962)	Oblate spheroid with 5:2 axial ratio
$\lambda_r$	Surface roughness factor	7	White et al. (1996)	Freshly comminuted silicates
$\rho$	Density	2.65 g/cm <sup>3</sup>	–	Density of quartz

silicate fraction (i.e. carbonate has been removed). Since all samples digested for major element analyses underwent the leaching procedures described above, all measured Ca derives from the silicate fraction. We also calculate the CIA (molar) from the molar oxide abundances (Goldberg and Humayun, 2010): CIA (molar) =  $\text{Al}_2\text{O}_3(\text{molar}) / (\text{CaO}^*(\text{molar}) + \text{Na}_2\text{O}(\text{molar}) + \text{K}_2\text{O}(\text{molar}))$ .

#### 2.4. Computational methods and U-series evolution codes

We simulate U-series isotopic evolution by numerically solving the equations outlined in the following section with codes written in the Julia programming language (Bezanson et al., 2017), available at <https://github.com/grahamedwards/ComminWeath.jl>. In these simulations we calculate fractional loss factors ( $f_{230}$  and  $f_{234}$ ) with Eq. (1b) and vary these values only by changing grain diameter ( $d$ ). We hold all other parameters constant, using values summarized in Table 2 (after Lee et al., 2010).

### 3. Theory and calculation

#### 3.1. Interpreting weathering histories from $^{230}\text{Th}$ - $^{234}\text{U}$ - $^{238}\text{U}$ compositions of multiple sediment fractions

The dependency of the post-communition U-series evolution of silts on the fractional loss factor (e.g. Fig. 3 and Eq. (2)) highlights the importance of accurately constraining the  $f_m$  term (Eq. (1)) in order to accurately simulate and interpret sedimentary U-series behavior. Yet, neither theoretical estimations of  $f_m$  (Lee et al., 2010) nor direct measurements of grain morphological properties (Handley et al., 2013) accurately and precisely determine this value. In this section, we present a novel approach to account for variability in the  $f_m$  value with  $^{230}\text{Th}$ - $^{234}\text{U}$ - $^{238}\text{U}$  systematics.

Assuming the idealized  $\alpha$ -recoil only model of Eq. (2), simulations of paired  $(^{230}\text{Th}/^{238}\text{U})$ - $(^{234}\text{U}/^{238}\text{U})$  compositions array nearly linearly for grain diameters  $\geq 10 \mu\text{m}$  and grain-shape parameters as in Table 2. While this relationship is not truly linear in a mathematical sense, it is effectively linear at the scale of analytical uncertainties ( $> 0.1\%$ ) for all  $f_m$  values representative of  $> 1 \mu\text{m}$  diameter grains, yielding regressions with coefficients of determination of  $r^2 > 0.999$  and modeled slopes varying by  $< 1\%$ . Thus, for a given comminution age, the  $(^{234}\text{U}/^{238}\text{U})$  and  $(^{230}\text{Th}/^{238}\text{U})$  values of chemically unaltered sediments should plot along isochrons, where older ages yield steeper slopes that converge on a maximal slope when grain size-controlled equilibrium is reached (Fig. 4). For sediments of a single age, the position of each fraction on the isochron is a function of its effective  $f_m$  values: a small  $f_m$  (large grain diameter) results in activity ratios close to unity, and a large  $f_m$  (small grain diameter) result in highly depleted activity ratios. Therefore, any variations among the free parameters used in calculating these  $f_m$  values only move compositions along the slope of the array, eliminating the need for a precise  $f_m$  value by matching multiple isotopic measurements with an  $f_m$ -independent trend.

In Taylor Valley, however, chemical alteration processes may obscure pristine detrital signals and perturb this theoretical comminution isochron. Thus, this approach of interpreting the  $^{230}\text{Th}$ - $^{234}\text{U}$ - $^{238}\text{U}$  systems of multiple sediment fractions with different grain sizes offers a new framework for interpreting the U-series evolutions of sediments in light of both physical and chemical weathering histories. While previous studies (Suresh et al., 2013; Cogez et al., 2018) have considered the

role of  $^{230}\text{Th}$  as a tracer of weathering processes in the interpretation of U-series  $\alpha$ -recoil processes, our approach is more similar to that used in chronological models of regolith chemical weathering (Dosseto et al., 2012; Chabaux et al., 2013) that fit generalized weathering parameters to  $(^{234}\text{U}/^{238}\text{U})$ - $(^{230}\text{Th}/^{238}\text{U})$  data. The present study unifies these two approaches to interpret  $(^{234}\text{U}/^{238}\text{U})$ - $(^{230}\text{Th}/^{238}\text{U})$  data with coupled physical and chemical weathering models that correspond to specific weathering processes. In the following section we introduce a quantitative model that explores dissolution-based weathering, authigenic effects, and  $\alpha$ -recoil processes, providing a more nuanced approach to interpreting these U-series systematics.

#### 3.2. Modeling $^{230}\text{Th}$ - $^{234}\text{U}$ - $^{238}\text{U}$ in fine particles in a physical and chemical framework

The following mathematical models build on equations for U-series comminution dating as well as regolith weathering models (Dosseto et al., 2012; Suresh et al., 2013; Chabaux et al., 2013). We assume that subglacial physical comminution is rapid and grain sizes are not further reduced (Haldorsen, 1981). We begin with the mathematical framework of Cogez et al. (2018), summarized in Eq. (3), that models  $\alpha$ -recoil ejection and loss to weathering. We treat chemical alteration of detrital silicate minerals as a bidirectional process, wherein U-series isotopes are not only removed by the dissolution of primary silicate phases (e.g. quartz and feldspar) but also added by authigenic mineral production. Our model tracks the evolution of the leach-insoluble sedimentary component, so meaningful authigenic replacement in this model is limited to silicate phases that are similarly leach-insoluble. Such authigenic silicates include amorphous silica, as observed in subglacial aqueous environments (Graly et al., 2020; Blackburn et al., 2019, 2020; Piccione et al., 2022), and clay minerals such as illite, smectite, and kaolinite, each of which are observed as chemical weathering products in Taylor Valley sediments (Marra et al., 2017).

We assume a constant weathering rate and 1:1 mass replacement of detrital quartz-feldspar minerals with leach insoluble authigenic phases. This simplifying assumption likely overestimates the effect but is approximately consistent with evidence for significant chemical silicate weathering in water-saturated MDV sediments (Lyons et al., 2021), abundant clay production in Antarctic subglacial systems (Graly et al., 2020), and observations of the Greenland ice sheet subglacial system, where twice the amount of rock represented as dissolved solute is precipitated as clay minerals (Graly et al., 2016). Furthermore, the  $^{230}\text{Th}$ - $^{234}\text{U}$ - $^{238}\text{U}$  compositions reported herein require significant addition of supra-SE material, not merely loss of U-series isotopes (see Section 4.3), justifying a model of efficient authigenic addition of  $^{230}\text{Th}$ - $^{234}\text{U}$ -enriched material.

To model this chemical replacement, we replace the weathering rate  $-kN_m$  terms in Eq. (3) with  $-kN_m^d + kN_m^a = k(N_m^a - N_m^d)$ , where the  $a$  and  $d$  superscripts respectively denote the authigenic and detrital phases of the simulated sediment. However, since chemical weathering occurs at the surface of particles, we scale  $k$  (in  $\text{g m}^{-2} \text{a}^{-1}$ ) by the specific surface area  $S$  (in  $\text{m}^2 \text{g}^{-1}$ ) calculated from Eq. (1c) for each modeled particle. While detrital material is being replaced by authigenic material within this model, we still consider this altered grain “detrital”, in contrast to a soluble authigenic rind.

We also explore the effects of U-series radionuclide implantation by  $\alpha$ -recoil from a high-U authigenic rind adjacent to the surface of the

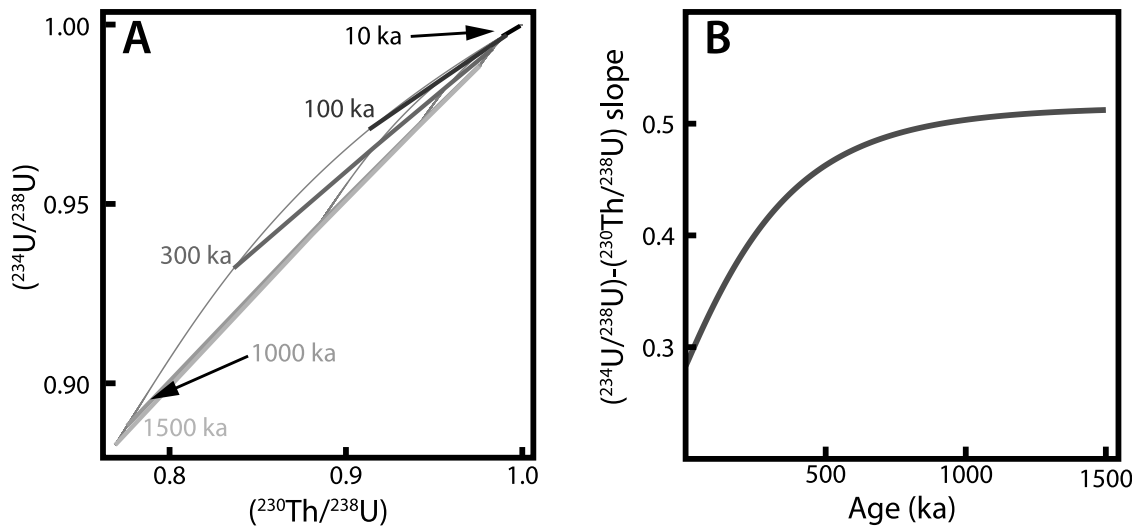


**Fig. 4.** Simulations of paired  $(^{230}\text{Th}/^{238}\text{U})$ - $(^{234}\text{U}/^{238}\text{U})$  systematics for chemically unaltered silt-sized particles following physical comminution. Numerical solutions to Eq. (2) for a given time ( $t$ ) produce a series of near-linear arrays for modeled grain diameters  $> 1 \mu\text{m}$  (A), each with a unique slope (B). Thin gray curves in panel A trace evolutions of individual simulated grains through time.

detrital grain. Prior studies have proposed the relevance of this  $\alpha$ -recoil process in U-series systematics of sedimentary systems (Lee et al., 2010; Plater et al., 1992; Menozzi et al., 2016). Tanaka et al. (2015) have shown that  $\alpha$ -recoil implantation of  $^{230}\text{Th}$  and  $^{234}\text{U}$  between phases in igneous rocks is common, and implanted nuclides are resilient to leaching with strong acid (6M HCl). On these grounds, we assert that this process is likely relevant in detrital-authigenic systems as well.

To quantitatively model implantation effects, we must first calculate an effective implantation factor for the authigenic rind that describes the fraction of  $\alpha$ -decays that result in both ejection from the rind and implantation into the detrital material, analogous to the fractional loss terms ( $f_m$ ) for  $\alpha$ -recoil loss. To accomplish this, we relate the specific surface area of the detrital component ( $S^d$ ) to the surface area of the authigenic rind ( $S^r$ , a specific surface area relative to the mass of the detrital component) scaled by the fraction of the sediment in contact with the rind ( $q$ ).

$$S^r = qS^d \quad (4)$$

Since the product of specific surface area and density is equivalent to the quotient of absolute surface area ( $A_S$ ) and volume ( $V$ ), or volumetric surface area,

$$S\rho = \left( \frac{A_S}{V} \right), \quad (5)$$

we can approximate  $S^r\rho^r$  using Eqs. (4) and (5) and a value  $z$  that represents the thickness of the authigenic rind.

$$S^r\rho^r = \frac{qS^d}{qS^d z} = \frac{1}{z} \quad (6)$$

By substituting Eq. (6) into Eq. (1a) we calculate a fractional implantation factor ( $f_m^{impl}$ ):

$$f_m^{impl} = \frac{L_m}{4z} \quad (7)$$

Thus, the rate of implantation of daughter nuclides (in moles) into the detrital component ( $N_m^d$ , where  $m$  is the daughter mass number) may be calculated from the molar abundance of the parent isotope in the rind ( $N_p^r$ , where  $p$  is the parent mass number) and its decay constant ( $\lambda_p$ ),

$$\frac{dN_m^d}{dt} = \frac{L_m}{4z} \lambda_p N_p^r, \quad (8)$$

And the authigenic rind ( $N_m^r$ ) itself may be modeled with

$$\frac{dN_m^r}{dt} = \left( 1 - \frac{L_m}{4z} \right) \lambda_p N_p^r \quad (9)$$

To simplify our calculations of the detrital grains, we use specific molar abundances (i.e. moles/gram) normalized to the mass of the detrital component. To convert specific molar abundance of the rind to a specific molar abundance relative to the mass of the detrital component we need the mass ratio of the authigenic ( $M^r$ ) and detrital ( $M^d$ ) components. Recalling that our parameters  $S^d$  and  $S^r$  are both normalized to the mass of the detrital component, we reformulate the mass-ratio with Eq. (4) such that

$$\frac{M^r}{M^d} = S^r z \rho^r = q S^d z \rho^r \quad (10)$$

Hence, we can rewrite Eq. (8) in terms of specific molar abundances (denoted with  $\hat{N}$  to differentiate from the  $N$  for absolute abundances):

$$\frac{d\hat{N}_m^d}{dt} = \frac{L_m}{4} \lambda_p \hat{N}_p^r (q S^d \rho^r) \quad (11)$$

with  $S^d$  calculated from Eq. (1c).

Including terms for chemical alteration and implantation, we rewrite Eqs. (3a)–(3c) in terms of specific molar abundances:

$$\frac{d\hat{N}_{238}^d}{dt} = S^d k_{238} (\hat{N}_{238}^a - \hat{N}_{238}^d) - \lambda_{238} \hat{N}_{238} \quad (12a)$$

$$\begin{aligned} \frac{d\hat{N}_{234}^d}{dt} = & S^d k_{234} (\hat{N}_{234}^a - \hat{N}_{234}^d) + \\ & \lambda_{234} \hat{N}_{234} + (1 - f_{234}) \lambda_{238} \hat{N}_{238} + \\ & [(L_{234}/4) q S^d \rho^r] \lambda_{238} \hat{N}_{238}^r \end{aligned} \quad (12b)$$

$$\begin{aligned} \frac{d\hat{N}_{230}^d}{dt} = & S^d k_{230} (\hat{N}_{230}^a - \hat{N}_{230}^d) + \\ & \lambda_{230} \hat{N}_{230} + (1 - f_{230}) \lambda_{234} \hat{N}_{234} + \\ & [(L_{230}/4) q S^d \rho^r] \lambda_{234} \hat{N}_{234}^r \end{aligned} \quad (12c)$$

We numerically solve Eqs. (12a)–(12c) to simulate the U-series evolutions of detrital particles that experience  $\alpha$ -recoil loss, authigenic replacement, and  $\alpha$ -recoil implantation. We explore the effects of these various processes on the U-Th isotopic compositions of silts from the Taylor-III drift in Section 4.4. In conclusion of this discussion, we note that  $f_m$  values, as calculated here, implicitly assume homogenous distribution of parent radionuclide throughout the modeled grain. While this is almost certainly the case for decay of  $^{238}\text{U}$  to  $^{234}\text{U}$ , as time progresses, the distribution of  $^{234}\text{U}$  becomes depleted in the outer  $\sim 35$  nm of grain radii, violating this assumption for calculations of  $^{234}\text{U}$  and  $^{230}\text{Th}$  and potentially resulting in inaccuracies. However,

**Table 3**

Chemical index of alteration (CIA) and CIA (molar) for fully leached sediments from Taylor Valley.

Drift	Grain size ( $\mu\text{m}$ )	CIA	$\pm 2\sigma$	CIA (molar)	$\pm 2\sigma$
Taylor I (englacial)	20–38	59.8	2.4	0.98	0.04
Taylor I (englacial)	20–38	60.7	2.4	1.01	0.04
Taylor III	75–125	61.8	2.8	1.06	0.05
Taylor III	38–45	62.3	2.9	1.07	0.05
Taylor III	20–38	61.4	2.5	1.03	0.04
Taylor III	10–20	61.6	2.8	1.06	0.05
Taylor IV	20–38	59.4	2.4	0.96	0.04
Taylor IV	10–20	56.3	2.6	0.84	0.04

overcoming this would require a geometrically complex model beyond the scope of the present study. We identify this as a key goal for future studies of sedimentary U-series systematics.

## 4. Results and discussion

### 4.1. Major element compositions and weathering indices

We report the chemical index of alteration, or CIA, and molar chemical index of alteration, or CIA (molar), for leached detrital (rapid Stokes settling) separates of Taylor Valley sediments in **Table 3** (raw major element data in Table S1, Supplementary Data). Traditional CIA values (after Nesbitt and Young, 1982) for detrital Taylor drift sediments are comparable to those calculated for bulk sediments (leached of carbonate and organic phases) of similar grain sizes ( $<63 \mu\text{m}$ ) collected proximal to the terminus of Howard Glacier in central Taylor Valley (Marra et al., 2017). However, while the CIA $>50$  compositions ought to imply evidence of weathering, this index is developed for intermediate to felsic rocks (Nesbitt and Young, 1982; Marra et al., 2017). Since the nearby Ferrar dolerite is a sediment source rock, the observed CIA $>50$  values may instead reflect the incorporation of anorthitic plagioclase feldspar grains (CIA=64.5). We instead focus on the CIA (molar), which provides a more generalized and quantitative measure of the degree of alteration from primary feldspathic material to more aluminous authigenic clays, such that pristine feldspars exhibit a CIA (molar)=1 that increases with increasing degree of alteration to clay minerals (Goldberg and Humayun, 2010).

Within this framework, CIA (molar) compositions indicate three different weathering regimes reflected in the three Taylor drift units (**Table 3**). Taylor-I fractions are within uncertainty of unity, reflecting limited major element evidence of chemical alteration. With one exception, the Taylor-III fractions are significantly elevated above 1, with no significant relationship between grain-size and degree of alteration. The Taylor-IV 10–20  $\mu\text{m}$  fraction exhibits a CIA (molar) composition significantly  $<1$ , while the 20–38  $\mu\text{m}$  fraction is  $\leq 1$ , indicating the presence of a subaluminous phase in the 10–20  $\mu\text{m}$  fraction. A carbonate phase is improbable given the extensive low-pH leaching treatments used (**Table 1**). Instead, given the proximity of the Taylor-IV drift units to outcroppings of Ferrar dolerite sills, we favor pyroxene or another mafic or calcic phase to account for this chemistry. While a denser phase such as this ought to have been removed by mineral separation methods, these methods may have been less efficient for finer grained separates due to slow settling rates in LST or particle adhesion. Therefore, the relationship between grain size and CIA (molar) in Taylor-IV may represent one of two things: either a lesser abundance of a subaluminous phase among coarser grain sizes or a greater degree of feldspar alteration to aluminous clay minerals. Given our inspection of mineralogic separates, we favor the latter explanation of a greater authigenic clay component, though we cannot definitively exclude the former. Finally, we acknowledge that clay minerals may also be inherited from the Beacon sandstones (Shaw, 1962), but collectively the CIA (molar) data show that little, if any, clay is incorporated into these “detrital” components of the Taylor drift sediments.

### 4.2. The effects of leaching

The leaching methods reduce U and Th concentrations of the residues relative to their unleached counterparts in all but two cases (Appendix **Table A.1**): the U concentration (hereafter [U]) of the leached fraction was higher than the unleached fraction in the finest Taylor-I detrital grains (10–20  $\mu\text{m}$ ) and the leached and unleached fractions of Taylor-IV clays had similar [U]. The former observation seems most likely explained by sample heterogeneity in a small aliquot from which only two fractions were available. In terms of  $^{230}\text{Th}$ - $^{234}\text{U}$ - $^{238}\text{U}$  data, leaching significantly altered the isotopic compositions of all detrital and clay size fractions with the exception of the 75–125  $\mu\text{m}$  size fractions. However, the directionality and magnitude of these changes varied widely from sample to sample and even among grain-size fractions within a sample (**Fig. 5**), indicating a broadly heterogeneous suite of leach-soluble phases that were effectively removed, leaving behind insoluble silicate residues. The notable exception to this is Taylor-IV, for which the  $(^{230}\text{Th}/^{238}\text{U})$  and  $(^{234}\text{U}/^{238}\text{U})$  of both leached and unleached fractions were similar for a given grain size. There was no significant effect on the composition of Taylor-I fractions leached three vs. five times, whereas additional leach iterations resulted in slightly lower  $(^{234}\text{U}/^{238}\text{U})$  compositions for Taylor-IV residues (Appendix **Table A.1**) that do not affect the overall interpretation of these data.

### 4.3. Overview of Taylor drift $^{230}\text{Th}$ - $^{234}\text{U}$ - $^{238}\text{U}$ data

In the following sections, we consider the compositions of leached residues, unless otherwise specified. Further, we follow the assumption that the hydraulic settling methods described in Section 2.2.1 effectively separated predominantly detrital silicate grains from predominantly authigenic clay silicate grains. For the sake of brevity, we refer to sediment aliquots that settled rapidly in water as “detrital” and those that settled more gradually as “clay”, though we recognize that clay minerals may be incorporated into the detrital component and vice versa.

The U-series compositions of detrital silt fractions all array approximately linearly (**Fig. 5**). While regressions of Taylor-III and -IV silts exhibit slopes within uncertainty of the steepest slopes predicted by a strictly physical weathering model (communition only), Taylor-I and -II slopes are significantly shallower than any predicted slope (**Fig. 4**).

Critically, all detrital fractions exhibit  $(^{230}\text{Th}/^{238}\text{U})>1$ , except for the finest (10–20  $\mu\text{m}$ ) Taylor-I silts, and only the Taylor-I detrital fractions and finest (10–20  $\mu\text{m}$ ) Taylor-IV detrital fraction exhibit  $(^{234}\text{U}/^{238}\text{U})<1$ . These observations refute an exclusively physical weathering history (**Figs. 3, 4**) and require significant alteration by authigenic processes. Although major element indices show limited evidence of chemical alteration, this process strongly perturbed the  $^{230}\text{Th}$ - $^{234}\text{U}$ - $^{238}\text{U}$  system, reflecting its sensitivity to both chemical and physical components of weathering. In the following sections, we interpret this U-Th data and infer the weathering histories for each Taylor drift units I, III, and IV (summarized in **Table 4**). The limited distribution of Taylor-II fractions in  $(^{234}\text{U}/^{238}\text{U})$ - $(^{230}\text{Th}/^{238}\text{U})$ -space prevent us from observing trends in its U-series evolution, so we only address it in the context of other drift units.

### 4.4. Taylor III: combined weathering and implantation effects

Taylor-III exhibits a range of relatively low-U (0.13–0.3  $\mu\text{g/g}$ ) that is positively correlated with grain size and negatively correlated with  $(^{234}\text{U}/^{238}\text{U})$  and  $(^{230}\text{Th}/^{238}\text{U})$  (**Figs. 6, 7**, Appendix **Table A.1**). The low U concentration of detrital fractions relative to clay and unleached fractions facilitates pronounced signals of grain-size dependent authigenic processes, indicated by the greatest enrichments of  $^{234}\text{U}$  and  $^{230}\text{Th}$  in the finest grains. Curiously, the array of detrital Taylor-III fractions appears to bifurcate among the finer grain sizes ( $<38 \mu\text{m}$ ) at

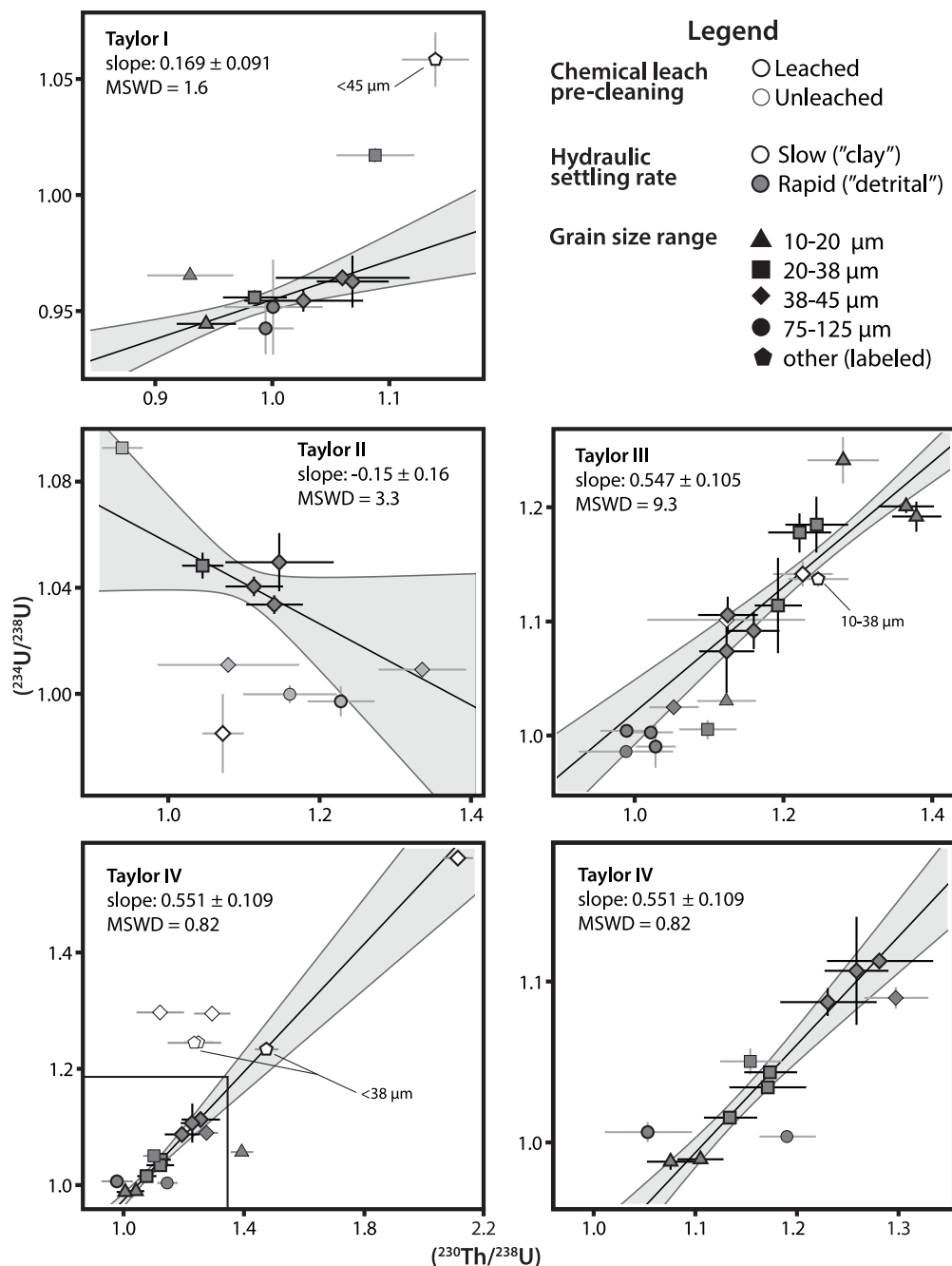


**Fig. 5.** U-series compositions of sediments from each Taylor Valley drift deposit. Maximum likelihood estimation regressions are calculated for leached,  $<50 \mu\text{m}$  diameter fractions of "detrital" quartz-feldspar separates (black error bars indicate inclusion in regression) and slopes are reported with the 95% confidence interval (calculated with IsoplotR Vermeesch, 2018). Note that Taylor IV is plotted twice on two different scales, and the inset box bounds the enlarged area.

**Table 4**

Summaries of U-series systematics and interpretations for Taylor Valley drift deposits I, III, and IV.

Drift	U-series systematics	Interpretations
Taylor-I	Narrow range of $(^{234}\text{U}/^{238}\text{U}) < 1$ for sands and silts. Broader range of $(^{230}\text{Th}/^{238}\text{U})$ . Inconsistent with trends from Taylor-III and -IV.	Minimal chemical alteration and U-series data indicate recent comminution within the last 100 ka.
Taylor-III	$[\text{U}]$ correlated positively with grain size and negatively with U-series activity ratios. All silts in excess of secular equilibrium. Bifurcating slope at finest grain sizes.	Significant role of $\alpha$ -recoil implantation, and variable role of authigenic replacement in fine-grained fractions. Weathering onset $>400$ ka.
Taylor-IV	$[\text{U}]$ negatively correlated with grain size and U-series activity ratios. U-series isotopes fall within a mixing envelope between Taylor-IV clay and Taylor-I detrital compositions.	Mixture between a detrital endmember and a clay endmember with U-series systematics dominated by $\alpha$ -recoil implantation over a $>1$ Ma weathering history.

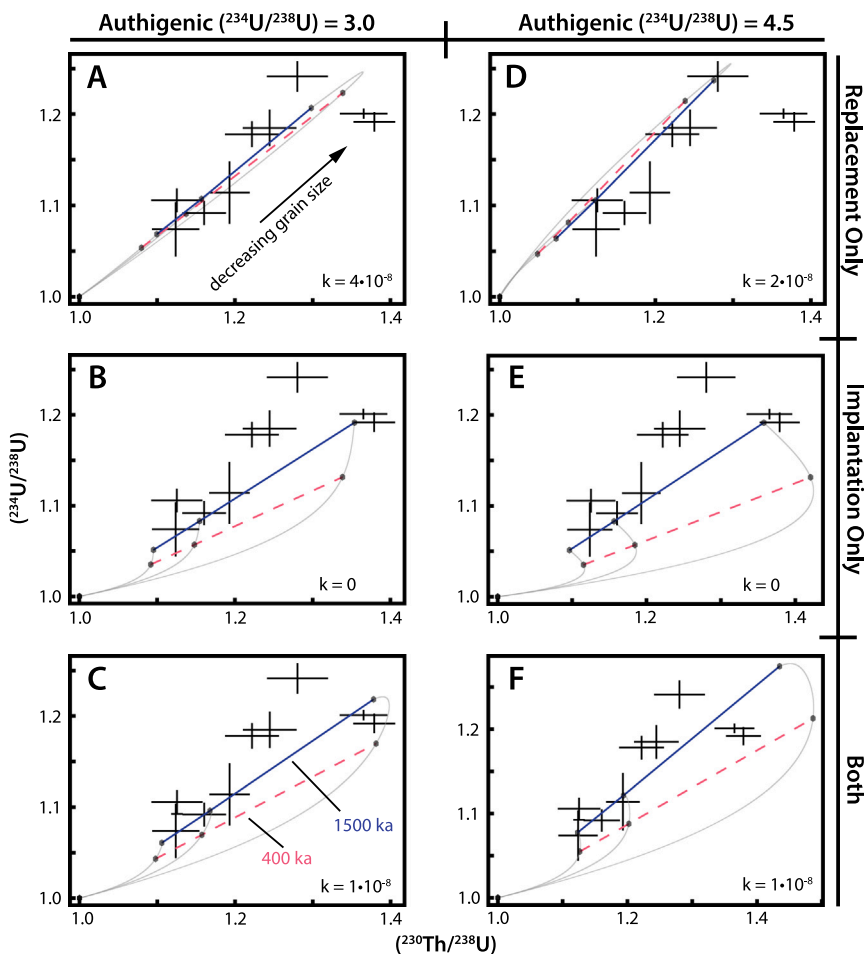


**Fig. 6.** Simulated detrital sediment  $^{230}\text{Th}$ - $^{234}\text{U}$ - $^{238}\text{U}$  systematics from a U-series chemical-physical weathering model compared to measured compositions of Taylor-III silts (black crosses trace  $2\sigma$  standard error). The panels define a grid of model conditions: columns correspond to modeled authigenic  $(^{234}\text{U}/^{238}\text{U})$  while rows correspond to the modeled chemical alteration processes. Panels A-C reflect authigenic  $(^{234}\text{U}/^{238}\text{U})=3.0$ . Panels D-F reflect authigenic  $(^{234}\text{U}/^{238}\text{U})=4.5$ . Panels A,D model only chemical replacement of detrital silicate with authigenic silicate, panels B,E model only  $\alpha$ -recoil implantation from a leach-soluble authigenic phase, and panels C,F incorporate both processes. Weathering rate coefficients ( $k$ , in  $\text{g m}^{-2} \text{ a}^{-1}$ ) are indicated in each panel. Additional parameters selected for each of these simulations are listed in Table 5. Gray curves trace the 1500 ka isotopic evolution of 15, 20, and 40  $\mu\text{m}$  diameter grains with isochronous arrays drawn at 400 ka (pink/dashed) and 1500 ka (blue/solid). Note that measured and simulated data both reflect negative correlations between  $(^{230}\text{Th}/^{238}\text{U})$  and grain-size.

high ( $^{234}\text{U}/^{238}\text{U}$ ) and ( $^{230}\text{Th}/^{238}\text{U}$ ), establishing a steeper-sloped subset and a shallower-sloped subset relative to the overall regression (Fig. 5). We explore these grain-size dependent processes and bimodal behavior using the mathematical framework of sediment U-series evolution from  $\alpha$ -recoil and chemical weathering processes outlined in Section 3.2.

#### 4.4.1. Model parameters

This section outlines and justifies the parameters chosen for the U-series physicochemical weathering model, summarized in Table 5. In all simulations, we assume initial detrital  $(^{234}\text{U}/^{238}\text{U}) = (^{230}\text{Th}/^{238}\text{U}) = 1$ , constrained by the measured composition of Taylor-III sand-sized fractions (75–125  $\mu\text{m}$ ), which are expected to be generally insensitive to grain-size dependent processes due to their larger size. In all simulations we assume a leach-insoluble authigenic [U] of 1  $\mu\text{g/g}$  based on the measured [U] of leached clay fractions (Appendix Table A.1) and a 2  $\mu\text{g/g}$  leach-soluble authigenic “rind” component that is a source of U-series radionuclide implantation. While we do not measure the [U] of the leach-soluble component directly, this estimate is reasonable in the context of the factor of 2–4 reduction in [U] after leaching, implying that the volumetrically small rind holds a large amount of U. Finally, we assume a 100 nm rind thickness in all implantation simulations. Output results are insensitive to rind thicknesses equal to or greater than this.

**Table 5**

Parameters used in simulations corresponding to each panel of Figs. 6 and 8.

Parameter	A	B	C	D	E	F	Fig. 8
Initial detrital ( $^{234}\text{U}/^{238}\text{U}$ )	1	1	1	1	1	1	0.94
Initial detrital ( $^{230}\text{Th}/^{238}\text{U}$ )	1	1	1	1	1	1	0.94
Authigenic ( $^{234}\text{U}/^{238}\text{U}$ )	3.0	3.0	3.0	4.5	4.5	4.5	3.0
Authigenic ( $^{230}\text{Th}/^{238}\text{U}$ )	4.6	4.6	4.6	4.6	4.6	4.6	–
Authigenic clay [U] ( $\mu\text{g g}^{-1}$ )	1	1	1	1	1	1	–
Soluble rind [U] ( $\mu\text{g g}^{-1}$ )	2	2	2	2	2	2	2
$k$ ( $10^{-8} \text{ g m}^{-2} \text{ a}^{-1}$ )	4	0	1	2	0	1	–
Proportion covered by rind	0	0.5	0.4	0	0.5	0.4	0.8
Rind thickness (nm)	0	100	100	0	100	100	$\geq 1000$

We vary the following parameters among the simulated scenarios: detrital [U], the authigenic weathering rate  $k$ , the proportion of the detrital component covered by an authigenic rind, and the  $^{230}\text{Th}$ - $^{234}\text{U}$ - $^{238}\text{U}$  composition of the authigenic components. In each simulated scenario we select initial detrital [U] compositions so that concentrations approach the measured values within the modeled timeframes. In the higher weathering scenarios ( $k > 1 \cdot 10^{-8}$ ), we use the same initial values for the sake of comparison, while in the case of nil authigenic weathering (implantation only), we simply use the measured [U] of

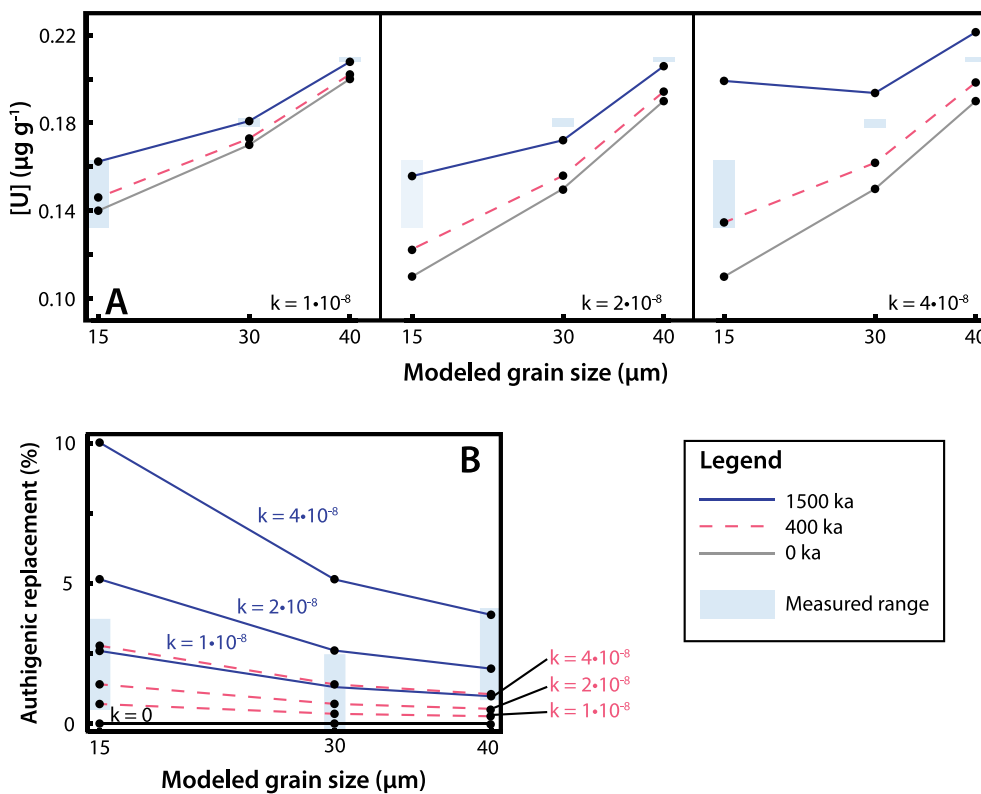


**Fig. 7.** Simulated sediment chemistries from model results in Fig. 6 compared to measured data from Taylor-III sediment fractions. (A) Modeled U concentrations at 0, 400, and 1500 ka for three different weathering coefficients ( $k$ , in  $\text{g m}^{-2} \text{ a}^{-1}$ ), corresponding to panels C and F ( $k = 1 \cdot 10^{-8}$ ), D ( $k = 2 \cdot 10^{-8}$ ), and A ( $k = 4 \cdot 10^{-8}$ ) in Fig. 6. Initial U were selected to match simulation results with observed U compositions for the  $k = 1 \cdot 10^{-8}$  and  $k = 2 \cdot 10^{-8}$  conditions by 1500 ka. The same initial U concentrations were used for the  $k = 2 \cdot 10^{-8}$  and  $k = 4 \cdot 10^{-8}$  scenarios for comparison. (B) Curves showing the molar percent of replacement of primary detrital silicate material with authigenic silicate material for each weathering coefficient scenario at 400 and 1500 ka. Measured ranges are calculated from chemical index of alteration values in Table 3 assuming an authigenic composition of illite, CIA(molar)=4. Note that any nil age condition or  $k = 0$  weathering condition yields no authigenic replacement.

Taylor-III detrital fractions as initial [U]. We select values for the authigenic weathering rate coefficient ranging  $0 \leq k \leq 4 \cdot 10^{-8}$  ( $\text{g m}^{-2} \text{ a}^{-1}$ ). The upperbound is comparable to the long-term ( $10\text{--}10^3$  ka) weathering rates applied to feldspars in Mediterranean climates (White et al., 1996). Although this climate is warmer than that of Taylor Valley, the weathering rate may be a reasonable approximation for water-saturated environments (Lyons et al., 1998; Marra et al., 2017; Lyons et al., 2021). We lack observations to constrain the proportion of the detrital grains covered by an authigenic rind, so we assume a proportion of 0.4–0.5, though this parameter may vary interchangeably with rind [U].

Since authigenic clays form by precipitation and aqueous alteration of primary silicates, authigenic clays likely incorporate the ( $^{234}\text{U}/^{238}\text{U}$ ) composition of local waters. We estimate the ( $^{234}\text{U}/^{238}\text{U}$ ) composition of the authigenic components from the aqueous compositions of Taylor Valley waters most likely to have interacted with these sediments. Given the elevation of Taylor-III at  $> 700$  m, this area has likely experienced little prolonged water residence since its deposition other than minor moisture from snowmelt (e.g. Campbell and Claridge, 1981) and deliquescence (Deutsch et al., 2022), which are poor sources of solutes (Lyons et al., 1998) but may scavenge U from the abundant soluble salts. Alternative sources of water at this location are either streamflow or flooding in an ice-marginal pond. Care was taken to sample far from any apparently fluvial sedimentary features, and the distance of this site from any alpine glaciers (the primary sources of streams in Taylor Valley) contradicts significant streamflow in this area (Fig. 1). We did not observe any field-based evidence of an ice-marginal pond at the sample site of the Taylor-III drift, but we cannot definitively preclude ponding during a prior high-stand of Taylor Glacier. Thus, the

aqueous history of the Taylor-III drift was likely dominated by small volumes of water from snowmelt and deliquescence, or perhaps an ice-marginal pond in the past.

To estimate the ( $^{234}\text{U}/^{238}\text{U}$ ) composition of the soil salts and/or theoretical ice-marginal pond, we infer that the major solute source to this pond would have been subglacial waters sourced from Taylor Glacier. These same fluids are observed today at Blood Falls and as groundwaters flowing into Lake Bonney bottomwaters (Mikucki et al., 2015). An ice-marginal pond might similarly tap into subglacial groundwaters as Lake Bonney does contemporaneously. Even without marginal ponding, Toner et al. (2013) showed that soil soluble salts in lower elevation Taylor Valley soils are the residues of evaporation at ancient paleolake highstands. Therefore, the most probable solute source for Taylor-III sediments was either the saline groundwaters or nearby lakewaters at the time of its deposition. Contemporary ( $^{234}\text{U}/^{238}\text{U}$ ) compositions of Lake Bonney range from  $\sim 3.0$  in the surface waters to  $\sim 4.5$  in the stratified deep waters and Blood Falls (Henderson et al., 2006). Water-lain precipitates from Taylor Valley record comparable enrichments over at least the last 400 ka (Hendy et al., 1979; Higgins et al., 2000). These values may be upper estimates given that ( $^{234}\text{U}/^{238}\text{U}$ ) decays with time, but  $^{234}\text{U}$  ejected from sediments by  $\alpha$ -recoil likely reduced this effect. After desiccation following drift deposition or evaporation of any ice-marginal waters, these salts might be routinely dissolved during snowmelt and deliquescence events and react with detrital material. Finally, since Th is insoluble,  $^{230}\text{Th}$  is likely readily available on the surface of grains due to its preferential adsorption to sediment surfaces after  $\alpha$ -recoil ejection or aqueous decay of  $^{234}\text{U}$ . In the absence of any measurements of  $^{230}\text{Th}$  in the Taylor Valley sedimentary environment, we assume  $(^{230}\text{Th}/^{238}\text{U})=4.6$  based off the value predicted from the Taylor-III regression for ( $^{234}\text{U}/^{238}\text{U}$ )=3.

#### 4.4.2. Model results

Fig. 6 presents the simulated  $^{230}\text{Th}$ - $^{234}\text{U}$ - $^{238}\text{U}$  isotopic evolutions for physically and chemically weathered sediments, while Fig. 7 summarizes the results for silicate-bound [U] and degree of authigenic replacement. Each simulation calculates the isotopic compositions of three model grain diameters (40, 30, 15  $\mu\text{m}$ ) through time, demarcating 400 ka and 1500 ka, at which point the system converges on an equilibrium state. The model simulates U-series response to  $\alpha$ -recoil ejection from detrital sediments, authigenic replacement of detrital minerals, and  $\alpha$ -recoil implantation into detrital material from a leach-soluble authigenic rind. This section outlines the latter two processes and compares the predicted effects to the measured U-series compositions of Taylor-III detrital fractions.

Panels A and D of Fig. 6 show the combined effects of  $\alpha$ -recoil ejection and authigenic replacement. As long as the rate of authigenic replacement exceeds the rate of  $\alpha$ -recoil loss of  $^{230}\text{Th}$  and  $^{234}\text{U}$ , the bulk grain compositions climb to  $(^{234}\text{U}/^{238}\text{U})$  and  $(^{230}\text{Th}/^{238}\text{U}) > 1$ . Due to the grain-size dependence of chemical weathering, for sediments of similar [U], the smaller grains characterized by larger surface area-to-volume ratios, are more affected and record higher  $(^{234}\text{U}/^{238}\text{U})$  and  $(^{230}\text{Th}/^{238}\text{U})$  than larger grains. Over the course of 1.5 Ma,  $(^{234}\text{U}/^{238}\text{U})$  and  $(^{230}\text{Th}/^{238}\text{U})$  increase to supra-SE values along an approximately constant slope (Fig. 6), controlled by the relative compositions of the authigenic  $(^{234}\text{U}/^{238}\text{U})$  and  $(^{230}\text{Th}/^{238}\text{U})$  composition. In both scenarios the corresponding slope and modeled array is consistent with the upper-bound slopes of Taylor-III silts (Fig. 6). However, the slopes are insensitive to time at the level of analytical uncertainties and thus provide little insight into the age of the sediments, although the weathering rates require a  $\ll 1.5$  Ma age to accommodate the observed CIA (molar) and [U] (Fig. 7).

Panels B and E of Fig. 6 explore the effects of only  $\alpha$ -recoil processes: implantation and ejection. For the modeled authigenic rind compositions, the modeled grains evolve through a broader isotopic space than the “replacement only” scenario, settling on values consistent with the measured data after nearly 1500 ka. While the replacement only scenario (Fig. 6A,D) reproduces the steeper sloped array at all timeframes, the “implantation only” scenario (Fig. 6B,E) effectively reproduces the shallower sloped array for  $> 400$  ka timeframes. Since the two modeled authigenic rinds only differ in initial  $(^{234}\text{U}/^{238}\text{U})$ , they converge on identical long-term behavior. By definition, this  $\alpha$ -recoil-only scenario includes no leach-insoluble (silicate) authigenic component and is inconsistent with the  $> 1$  CIA (molar) compositions of Taylor-III silts (Fig. 7, Table 3), unless these compositions reflect peraluminous detrital material or inherited clays from Beacon sandstone cements (Shaw, 1962).

Panels C and F of Fig. 6 explore the combined effects of authigenic replacement,  $\alpha$ -recoil implantation, and  $\alpha$ -recoil ejection. The modeled arrays begin to intersect the measured values shortly after 400 ka and the long-term equilibria lie within the two endmember slopes. Thus, within 400–1500 ka the combined model reproduces observed isotopic compositions, [U], and CIA (molar) compositions (Figs. 6, 7).

#### 4.4.3. Preferred weathering history for Taylor-III sediments

In terms of  $(^{230}\text{Th}/^{238}\text{U})$  and  $(^{234}\text{U}/^{238}\text{U})$  compositions, the authigenic replacement-only endmember model satisfies the observed data that array a steeper slope after  $\geq 400$  ka, whereas the implantation-only endmember satisfies the shallower-sloped data for 400 to  $> 1500$  ka (Fig. 6). However, the two-endmember scenarios of chemical weathering respectively invoke exclusively leach-insoluble and leach-soluble chemical weathering products, resulting in predicted degrees of silicate chemical alteration that respectively overestimate and underestimate the CIA (molar) of the measured data (Fig. 7). While neither endmember scenario is able to independently satisfy the observed Taylor-III detrital sediment compositions, a combination of the two scenarios satisfies all of the observed data (Figs. 6, 7).

While some degree of chemical alteration is implied by CIA (molar) values, we emphasize two key evidences for a significant role of  $\alpha$ -recoil implantation from a high-U authigenic phase into the lower-[U] detrital phase. First, several  $< 38 \mu\text{m}$  detrital grains exhibit more-enriched  $(^{230}\text{Th}/^{238}\text{U})$  and  $(^{234}\text{U}/^{238}\text{U})$  compositions than corresponding clay fractions, implying an additional  $^{230}\text{Th}$ - and  $^{234}\text{U}$ -enriching process beyond clay precipitation. Second, the unleached fractions have higher [U] but lower  $(^{230}\text{Th}/^{238}\text{U})$  and  $(^{234}\text{U}/^{238}\text{U})$  compositions than their leached equivalents (Fig. 5), indicating complimentary reservoirs of high- and low-U that have exchanged  $^{230}\text{Th}$  and  $^{234}\text{U}$  (Tanaka et al., 2015; Menozzi et al., 2016). Because high-U authigenic rinds are likely very thin (e.g.  $< 1 \mu\text{m}$ ), we expect that their  $f_m$  values were extremely high, and the rinds efficiently lost  $^{230}\text{Th}$  and  $^{234}\text{U}$  to  $\alpha$ -recoil on geologic timescales. Since a large proportion of the rind’s  $\alpha$ -recoil ejections are adjacent to the detrital grain surface, those implanted isotopes raised the  $(^{230}\text{Th}/^{238}\text{U})$  and  $(^{234}\text{U}/^{238}\text{U})$  of the detrital grain while lowering these compositions in the soluble rind.

At  $< 38 \mu\text{m}$  grain sizes, Taylor III silts split into two groups of steeper and shallower slope. Histories dominated by authigenic clay formation favor the steeper slope, whereas implantation-dominated processes favor the shallower slope. We interpret this bifurcating array to reflect heterogeneity in the effective contribution of implantation and replacement at fine-grained sizes that are most sensitive to these processes: grains more affected by authigenic replacement trend to the steeper slope endmember, while those more affected by implantation trend toward the shallower slope. The combination of these two processes obfuscates any temporal information about the physical or chemical weathering history other than an onset of weathering processes prior to 400 ka, consistent with the depositional age (Fig. 2). Similarly, we note that the preferred scenarios presented in this section do not uniquely explain the observed data, and minor adjustments to the chosen parameters can fine-tune a variety of weathering histories to match measured compositions. However, the model results do show conclusively that the U-series compositions of Taylor-III detrital silts require a combined authigenic alteration and  $\alpha$ -recoil implantation history (Fig. 6).

#### 4.5. Taylor-IV: mixing between detrital and authigenic endmembers

The line regressed to fit the detrital fractions of Taylor-IV intersects clay fractions at  $(^{234}\text{U}/^{238}\text{U})$  and  $(^{230}\text{Th}/^{238}\text{U})$  compositions  $\sim 5$  times as enriched above SE, even though they were not included in the regression (Fig. 5). Extrapolating this line to lower values, it also intersects Taylor-I detrital grains, implying a plausible isotopic relationship among these three components. Indeed, a mixing envelope mapped between Taylor-I detrital and Taylor-IV clay components in the 10–38  $\mu\text{m}$  grain diameter range, comfortably overlaps all other Taylor-IV fractions and the Taylor-I clay fraction (Fig. 8A, B). All  $> 20 \mu\text{m}$  Taylor IV fractions also fall within the bounds of a mixing envelope bounded by the Taylor-I 38–45  $\mu\text{m}$  fractions and the corresponding grain size of the Taylor-IV clay component (Fig. 8A, B).

The two-endmember mixing model is supported by the relationships among [U], grain size, and isotopic ratios:  $(^{234}\text{U}/^{238}\text{U})$  and  $(^{230}\text{Th}/^{238}\text{U})$  scale with grain size, while [U] is negatively correlated with each (Fig. 5, Appendix Table A.1). Thus, the highest-[U] ( $\sim 1.3 \mu\text{g/g}$ ) 10–20  $\mu\text{m}$  Taylor-IV fractions lie closest to the Taylor-I detrital endmember, while the lowest-[U] ( $< 0.15 \mu\text{g/g}$ ) 38–45  $\mu\text{m}$  Taylor-IV fractions are more strongly leveraged by mixing with a high- $(^{230}\text{Th}/^{238}\text{U})$ - $(^{234}\text{U}/^{238}\text{U})$  clay-like endmember (Figs. 5, 8). Incorporation of a clay-like endmember is also consistent with the higher CIA (molar) value for coarser Taylor-IV detrital grains, implying that these reflect a higher clay component than their finer-grained counterparts (Table 3). Curiously, Taylor-IV sands (75–125  $\mu\text{m}$ ) are decoupled from this trend with a [U] comparable to the 38–45  $\mu\text{m}$  size fraction but  $(^{234}\text{U}/^{238}\text{U}) \sim (^{230}\text{Th}/^{238}\text{U}) \sim 1$  (Fig. 5, Appendix Table A.1), likely

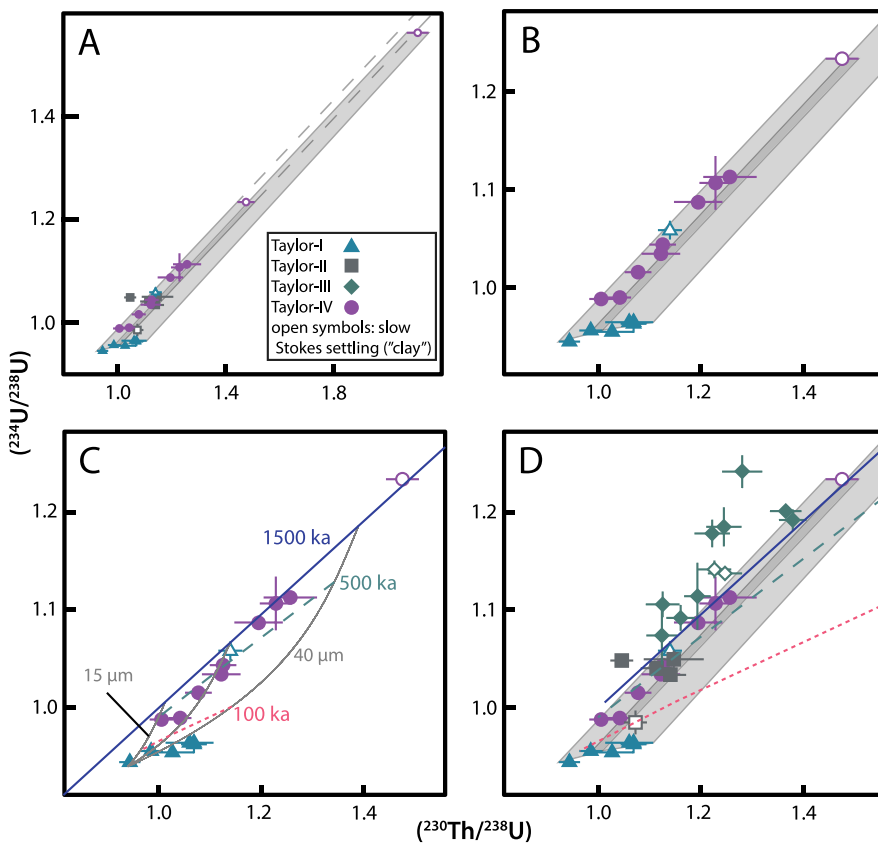


**Fig. 8.** Mixing relationships among Taylor-I, -II, and -IV drifts in  $(^{230}\text{Th}/^{238}\text{U})$ - $(^{234}\text{U}/^{238}\text{U})$  space, emphasizing mixing between a detrital Taylor-I endmember and clay Taylor-IV endmember. Filled symbols represent detrital quartz-feldspar fractions and open symbols represent clay fractions. (A,B) Mixing envelopes (gray) bounding the Taylor-I detrital endmember and Taylor-IV clay endmembers for 10–38  $\mu\text{m}$  and 38–45  $\mu\text{m}$  grain diameters. Dashed lines in A extrapolate the 10–38  $\mu\text{m}$  grain size envelope. Taylor-IV detrital fractions and the T-I clay fraction overlap these envelopes. (C) Isotopic evolution curves (gray) and isochronous arrays (100, 500, 1500 ka) for a simulated history of  $\alpha$ -recoil implantation from a soluble authigenic coating. The assumed model parameters are listed in Table 5. (D) Mixing envelopes from A-B and extrapolated arrays from C, including all leached detrital and authigenic silicate fractions from Taylor drifts I-IV.

reflecting both a lesser clay contribution and relative insensitivity to grain-size dependent  $\alpha$ -recoil processes at this size range.

The two-endmember mixing model coherently and parsimoniously explains the Taylor-IV data topology, though it does not explicitly identify the underlying mechanisms. The high- $(^{234}\text{U}/^{238}\text{U})$ - $(^{230}\text{Th}/^{238}\text{U})$  Taylor-IV clay endmember tempts the interpretation that efficient aqueous authigenic processes are contributing high- $^{230}\text{Th}$  and  $^{234}\text{U}$  phases (clay or amorphous silica) to detrital silicates. Yet, abundant authigenic mineral production seems improbable in the case of Taylor-IV. First, all simulations of authigenic replacement failed to reproduce the slope and topology of Taylor-IV data for any combination of input parameters. More importantly, given the >1.5 Ma depositional age (Wilch et al., 1993) of Taylor-IV, ancient products of chemical alteration would return to SE (or lower) unless routinely refreshed over this long time-frame. Therefore, sustaining the elevated  $(^{234}\text{U}/^{238}\text{U})$  and  $(^{230}\text{Th}/^{238}\text{U})$  compositions of Taylor-IV by authigenic replacement alone requires one of the following scenarios: frequent interaction with moderately high [U] and  $(^{234}\text{U}/^{238}\text{U})$  waters or interaction within <<1.5 Ma with very high [U] and/or  $(^{234}\text{U}/^{238}\text{U})$  waters similar to the subglacial waters and groundwaters of Taylor and Wright Valleys (Henderson et al., 2006). We reject the first scenario of frequent interaction with waters due to the abundant soluble salts in Taylor-IV sediments (Bockheim, 2002) that would be removed if they were frequently flushed with water (e.g. Lyons et al., 2021). The second scenario is similarly implausible, requiring transport of subglacial waters or lake bottom waters to heights of 1 km above where they are observed today. Expansions of lakes have not exceeded 400 m elevation in the last several hundred

thousand years (Hall et al., 2000) and the nearby Taylor Glacier margin has not reached an elevation within 150 meters of the sample location in > 450 ka (Fig. 1).

In the absence of significant authigenesis, the only viable mechanism to sustain the high- $(^{234}\text{U}/^{238}\text{U})$ - $(^{230}\text{Th}/^{238}\text{U})$  compositions of Taylor-IV sediments is  $\alpha$ -recoil implantation of  $^{230}\text{Th}$  and  $^{234}\text{U}$  by an adjacent soluble and high-U phase. Indeed, a long-term implantation simulation approximately reproduces the trend of the Taylor-I-IV mixing envelope (Fig. 8). In Section 4.6 we show that Taylor-I sediments are recently comminuted, so we choose the composition of Taylor-I silts as the initial composition, but the long-term (1500 ka) condition is independent of the chosen initial  $(^{234}\text{U}/^{238}\text{U})$  and  $(^{230}\text{Th}/^{238}\text{U})$  conditions. The extrapolated trend intersects Taylor-IV's <38  $\mu\text{m}$  clay fraction and nearly intersects the highly-enriched 38–45  $\mu\text{m}$  clay fraction. We expect clays to sensitively record implantation due to the large surface area-to-volume ratios of clay minerals and weathered detrital silicates (e.g. Marra et al., 2017). Thus, we propose that the mixing envelope reflects mixture between a detrital endmember, which may or may not be affected by  $\alpha$ -recoil implantation, and a clay endmember with U-series systematics dominated by  $\alpha$ -recoil implantation. This model predicts an increasing clay component among the lower-[U] and coarser-grained detrital fractions of Taylor-IV silts that is consistent with the CIA (molar) trend (Table 3).

This model implies that the 38–45  $\mu\text{m}$  Taylor-II fractions (detrital and clay) and Taylor-I clay fraction may also incorporate ancient clays from the Taylor-IV drifts (Fig. 8D). These ancient clays may have been transported to lower elevation drifts either by efficient down-valley

aeolian transport (Diaz et al., 2018) or colluvial processes. Incorporating these clay materials into Taylor Glacier basal ice merely requires transport of the clay to the upper Taylor Valley floor during Marine Isotope Stage 2 when Taylor Glacier was at a reduced extent (Higgins et al., 2000). The inability of Stokes settling and aggressive leaching methods to separate clay materials from the Taylor-II and -IV detrital components indicates that these authigenic phases readily adhere to detrital quartz and/or feldspar surfaces, resisting removal by vigorous physical agitation as well as chemical attack (Cogez et al., 2018). In contrast, Taylor-III fractions (detrital and clay) require an additional authigenic replacement component (Section 4.4) and are not satisfied by this mixing envelope and corresponding implantation history, alone (Fig. 8).

We propose that the abundant and widespread soluble salts found in Taylor-IV soils (Bockheim, 2002) as the most probable candidate for the high-U authigenic phase responsible for the  $\alpha$ -recoil implantation histories recorded in Taylor-IV sediments. Unlike Taylor-III, the leached and unleached fractions of Taylor-IV sediments have comparable  $^{230}\text{Th}$ - $^{234}\text{U}$ - $^{238}\text{U}$  compositions (Fig. 5), implying that  $\alpha$ -recoil implantation affected both authigenic and detrital phases similarly. Therefore, this adjacent high-U phase must have been removed before the sediments were exposed to leaching reagents. High salt contents have been observed in sediments collected near the Taylor-IV sample site and the high aqueous solubility of the soil salts in Taylor Valley ensure that they would have been efficiently removed during wet-sieving and Stokes settling procedures (Toner et al., 2013). Indeed, we observed salt residues in the dehydrated supernatant waters of these experiments. Unfortunately, we did not preserve these salts and cannot directly test the hypothesis that these soil salts reflect a [U] in sufficient excess of the detrital fractions (i.e.  $>1 \mu\text{g/g}$ , Appendix Table A.1) to account for the observed degree of  $\alpha$ -recoil implantation. However, since these salts were likely sourced from subglacial or proglacial waters that later evaporated (Toner et al., 2013), this high-U hypothesis is supported by analogous salt material. Proglacial soluble salts (nahcolite, trona) from Lewis Cliff, Antarctica approach  $1 \mu\text{g/g}$  U (Fitzpatrick et al., 1990). Taylor Valley salts are likely even more U-rich, given local gypsum precipitated from Holocene Lake Bonney with  $2\text{--}3 \mu\text{g/g}$  U and Holocene to  $> 400$  ka carbonates that are typically  $> 10 \mu\text{g/g}$  U (Hendy et al., 1979).

#### 4.6. A comminution age for Taylor I silts

The detrital fractions of Taylor-I reflect a narrow range of sub-SE ( $^{234}\text{U}$ / $^{238}\text{U}$ ) compositions (0.94 to 0.97) for all grain sizes, while ( $^{230}\text{Th}$ / $^{238}\text{U}$ ) vary more broadly from 0.9 to 1.1 (Fig. 5). These fractions lie along a shallow-sloped array that is not consistent with mixing with a Taylor-IV clay endmember (Fig. 8) but may reflect a mixture between a sub-SE ( $^{234}\text{U}$ / $^{238}\text{U}$ ) and ( $^{230}\text{Th}$ / $^{238}\text{U}$ ) detrital endmember and a higher- $^{230}\text{Th}$  endmember. Because [U] varies from 0.2 to  $1.6 \mu\text{g/g}$  between the  $>20 \mu\text{m}$  and  $10\text{--}20 \mu\text{m}$  fractions, respectively, the finest size fraction provides a best estimate for the U-series isotopic composition of the unaltered Taylor-I detrital component. This significantly sub-SE  $^{230}\text{Th}$ - $^{234}\text{U}$ ,  $^{238}\text{U}$  composition independently suggests ancient physical comminution under the framework of U-series comminution dating (Fig. 4). However, the ( $^{234}\text{U}$ / $^{238}\text{U}$ ) is indistinguishable from the  $75\text{--}125 \mu\text{m}$  fraction, which should be insensitive to grain-size-dependent  $\alpha$ -recoil processes, suggesting that this sub-SE composition may instead be an inherited property from the source rock or a product of grain-size-independent weathering processes.

The canonical assumption in U-series comminution dating that freshly comminuted sediments are in SE has not been systematically confirmed. Despite widespread observations of SE in  $\geq 1.5$  Ma rocks, the rapid release of U with ( $^{234}\text{U}$ / $^{238}\text{U}$ )  $> 1$  from freshly comminuted granite to pore solutions implies that internal  $\alpha$ -recoil damage to silicate matrices prior to comminution may leave atoms of radiogenic  $^{234}\text{U}$  and  $^{230}\text{Th}$  effectively labile when recoil-damaged zones are exposed to

chemical weathering environments following comminution (Andersen et al., 2009). Under such a model, grains comminuted from ancient bedrock converge on grain-size controlled sub-SE compositions shortly after comminution (Fig. 9). If true, this model implies that radionuclides implanted by  $\alpha$ -recoil after comminution (i.e. Taylor-III, -IV) may be more resilient to leaching than radionuclides in  $\alpha$ -recoil damaged zones exposed by comminution (i.e. Taylor-I). Alternatively, lithologic or morphologic differences between the Taylor-I and other Taylor drift sediments may account for different behavior in the damaged zones of these particles, supported by the sand-sized grains with ( $^{234}\text{U}$ / $^{238}\text{U}$ )  $\sim 1$  in Taylor drifts II-IV. Though we lack the data to substantively test this model in the present study, these observations appear to undermine a fundamental assumption of U-series comminution dating that pre-comminution  $\alpha$ -recoil processes do not affect post-comminution  $\alpha$ -recoil behavior.

Although U-series isotopes fail to resolve the timescales of Taylor-I physical weathering, the limited degree of chemical alteration observed in detrital Taylor-I sediments strongly support recent, rather than ancient, physical comminution. We predict efficient aqueous chemical alteration, likely enhanced by microbial activity (Montross et al., 2013), in the basal and subglacial environment of Taylor Glacier. This prediction is supported by evidence for subglacial aquatic environments beneath Taylor Glacier (Hubbard et al., 2004; Mikucki et al., 2015), microbial activity in subglacial waters (Mikucki et al., 2009) and basal ice (Montross et al., 2014), and efficient aqueous chemical weathering in Taylor Valley groundwaters (Lyons et al., 2021). Yet, with a CIA (molar) composition within  $\leq 1\sigma$  of unity, the Taylor-I sediments extracted directly from this regime show no major-elemental evidence of primary silicate replacement with aluminous clay minerals like Taylor-III silts do (Table 3). While amorphous  $\text{SiO}_2$  coatings may contribute authigenic material without raising the CIA (molar), there is no reason to expect that the subglacial aqueous environment of Taylor Glacier would accommodate significant precipitation of amorphous  $\text{SiO}_2$  without concomitant clay precipitation. U-series isotopes reinforce the limited extent of chemical alteration in Taylor-I sediments. Taylor-I clays fall on the mixing line between the detrital Taylor-I component and the high- $(^{234}\text{U}$ / $^{238}\text{U}$ )- $(^{230}\text{Th}$ / $^{238}\text{U}$ ) clay component of Taylor-IV (Fig. 8A, B), suggesting that any extant clays were inherited from upslope Taylor-IV deposits (Section 4.5). Yet, the Taylor-I detrital components cannot be inherited or they would exhibit compositions of a Taylor-II-IV detrital silt. Rather they reflect an endmember composition within a relatively limited range of ( $^{234}\text{U}$ / $^{238}\text{U}$ ) and ( $^{230}\text{Th}$ / $^{238}\text{U}$ ), showing no evidence of appreciable U gain by authigenic processes and only limited  $^{230}\text{Th}$  gain that varies distinctly from the more altered sediments of the drift sheets.

By all metrics, Taylor-I sediments reflect far less evidence of chemical weathering than any of the Taylor drift sheet sediments (II-IV). Prior to freeze-on to the base of Taylor Glacier, Taylor-I sediments resided in reactive subglacial and proglacial waters. Taylor-III and Taylor-IV sediments, on the other hand, are perched hundreds of meters above the modern valley floor in a hyper-arid environment. If all Taylor Valley sediments were comminuted before 1.5 Ma, then Taylor-I should be at least as altered as the older drift units. In the absence of any such evidence of weathering within the Taylor-I detrital fraction, we must accept a history of recent physical weathering and only brief chemical weathering.

#### 4.7. The coupled physical-chemical weathering history of Taylor valley

The major-element and U-series evidence of limited chemical weathering in Taylor-I detrital sediments requires comminution more recent than the Taylor-III drift unit, which was deposited at least 400 ka. If we assume its lowest ( $^{234}\text{U}$ / $^{238}\text{U}$ )- $(^{230}\text{Th}$ / $^{238}\text{U}$ ) measurements as an initial composition, the array of Taylor-I detrital grains is consistent with a  $<100$  ka evolution controlled by  $\alpha$ -recoil implantation (Fig. 8). This age disparity between drift deposits and currently entrained sediments

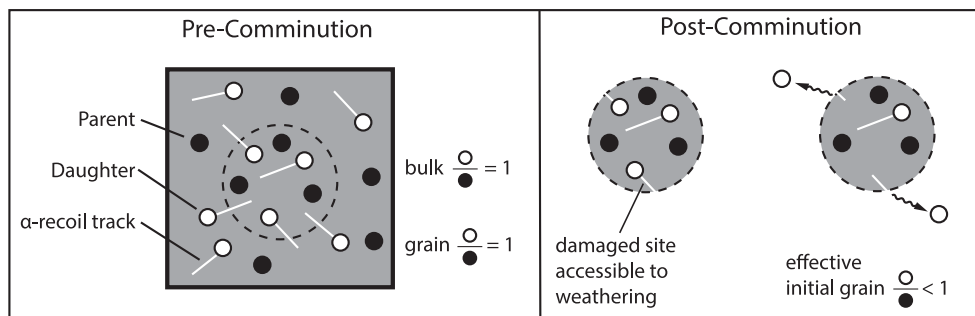


**Fig. 9.** Diagram of the proposed process of rapid daughter (e.g.  $^{234}\text{U}$ ) loss following comminution. Prior to comminution,  $\alpha$ -recoil events damage the mineral lattice around daughter isotopes, leaving “ $\alpha$ -recoil tracks”. Following comminution, those damaged zones are more susceptible to weathering, allowing for the rapid loss of daughter isotopes with  $\alpha$ -recoil tracks intersecting the grain surface.

provides robust support for the ongoing production of fine particles by mechanical wear processes beneath Taylor Glacier, likely facilitated by basal sliding in sub-solidus basal zones (e.g. Hubbard et al., 2004). Active mechanical wear, in turn, implies active glacial incision in Taylor Valley that continued through the Pleistocene and perhaps continues today. Although our results do not quantify the extent of Pleistocene incision, they contradict canonical models of universally stagnant MDV landscapes over the last  $> 15$  Ma (Denton et al., 1993; Sugden and Denton, 2004). Rather, we interpret that Taylor Glacier behaves more like warm-based outlet glaciers (e.g. Mackay Glacier) that actively denude the valleys they occupy (Sugden and Denton, 2004) and contribute to the extreme relief within the Trans-Antarctic Mountains (Stern et al., 2005). While unglaciated high elevations likely reflect very ancient landscapes that have experienced little alteration over millions of years (Brook et al., 1995), our results emphasize that Antarctic glaciers with subglacial brine like Taylor Glacier are likely candidates for lubricated basal conditions, slow sliding, and gradual valley incision.

We use simple calculations to argue for the plausibility of glacial valley incision during the Quaternary. Modern Taylor Glacier has a surface velocity of  $\sim 10$  m/yr (Kavanaugh et al., 2009), though different studies conclude different movement mechanisms between the upper glacier (Kavanaugh and Cuffey, 2009) and its terminus (Pettit et al., 2014). More recently, the presence of liquid brine has been shown at least beneath the lower part of Taylor Glacier (Mikucki et al., 2015). This suggests that some basal sliding is occurring despite the cold nature of the glacier ice in the study area (see also Cuffey et al., 1999), albeit at rates so low that they have been difficult to detect using inverse modeling of glacier flow (Kavanaugh and Cuffey, 2009; Pettit et al., 2014). While recognizing these uncertainties, in our calculations we assume a sliding velocity of the order of 1 m/yr, which is about 10% of the observed ice surface velocity of Taylor Glacier. A simple and commonly used rule for subglacial erosion rates assumes that they scale linearly with basal sliding velocity by a non-dimensional proportionality coefficient of  $\sim 0.0001$  (e.g. MacGregor et al., 2000). This rule suggests a subglacial erosion rate of 0.1 mm/yr for a basal sliding velocity of 1 m/yr. At this rate, subglacial erosion would deepen the valley floor beneath Taylor Glacier by 100 m/Ma. If the fraction of Taylor Glacier’s surface velocity accommodated by basal sliding is  $> 10\%$ , the long-term erosion rate may be several hundred meters per Ma. Conversely, a smaller sliding fraction indicates an incision rate of tens of meters per Ma or less.

We separately examine the feasibility of glacial incision beneath Taylor Glacier by estimating a subglacial erosion rate from the modern debris flow to its terminus. The very fact that sediment is discharged at the glacier front supports the contention that erosion is occurring at some rate beneath this glacier. We estimate the sediment flux rate per unit width of the glacier by multiplying the ice velocity by an average thickness of basal debris-bearing ice and an average sediment

concentration. Near the terminus, the glacier moves at  $\sim 5$  m/yr (Pettit et al., 2014). Basal ice thickness is more difficult to determine because much of the glacier terminus is submerged in Lake Bonney. Spigel et al. (2018) used data from an autonomous underwater vehicle (AUV) to infer that lake water is in contact with glacier ice to a depth of nearly 25 m below the lake surface. AUV footage of the glacier front showed variable topography of the ice surface, consistent with the ice being debris laden. Based on these observations, we assume a relatively large basal ice thickness of 20 m, which is close to the 10–15 m estimate from inverse modeling by Pettit et al. (2014). Volumetric debris concentrations in the basal ice of Taylor Glacier, as in general, vary from as low as  $\sim 0.1\%$  to as high as tens of percent (Knight et al., 2002; Montross et al., 2014; Fitzsimons et al., 2024). We use a range of 1%–10% volumetric debris content to estimate a debris flux of 1–10  $\text{m}^3/\text{yr}$  per meter of glacier terminus width. If this debris is incorporated into the basal ice along a  $\sim 100$  km glacier flowline, we obtain a subglacial erosion rate of 0.01 to 0.1 mm/yr by dividing the debris flux by the length of the flowline. We note that flowline width crudely scales with the width of the glacier, which varies by a factor of a few along its length (e.g. Kavanaugh et al., 2009). Since this variability is significantly smaller than the uncertainty in the mean debris concentration, we conclude that flowline width variation likely has a limited impact on our order-of-magnitude estimates. While we acknowledge various uncertainties associated with these calculations, our estimates of erosion from debris flux and sliding velocities both support long-term erosion rates of tens to hundreds of meters per Ma.

Our results indicate chemical weathering histories no-less dynamic than those of physical weathering. The U-series systems of three drift deposits and sediments entrained in basal ice record a variety of chemical alteration processes that have varied as a function of both time and weathering environment. With the exception of more recently comminuted sediments (Taylor-I), enrichments of U-series intermediate daughter nuclides  $^{230}\text{Th}$  and  $^{234}\text{U}$  in silicate sediments are commonplace and comparable to many of the enrichments observed in surface waters (Henderson et al., 2006). These enrichments indicate that  $\alpha$ -recoil processes have directly and indirectly influenced the isotopic evolutions of sediments in the various Taylor Glacier drift sheets. The ancient deposition, high elevation above the valley floor, and extensive salt accumulations of the Taylor-IV deposit refute any recent or routine aqueous alteration processes. U-series compositions instead indicate a  $> 1$  Ma duration of  $\alpha$ -recoil implantation from an adjacent uraniferous phase that preferentially affected high-surface area clay fractions (Fig. 8). The implanting phase was very likely the abundant water-soluble salts that cement many of these ancient drift deposits (Bockheim, 2002). In contrast, the U-series systematics of Taylor-III are more consistent with minor authigenic clay production in addition to  $\alpha$ -recoil implantation, suggesting more recent/frequent contact with water than the higher elevation Taylor-IV deposits. Since the unleached fractions of Taylor-III reflect significantly lower ( $^{234}\text{U}/^{238}\text{U}$ )

and ( $^{230}\text{Th}/^{238}\text{U}$ ) compositions than fine-grained ( $<38\ \mu\text{m}$ ) leached fractions (Fig. 5), the leach-soluble phases may have been an implanting phase. However, the supra-SE compositions of unleached fractions imply a contribution from soluble salts, as well.

In the hyperarid high-elevation environments of Taylor Valley,  $\alpha$ -recoil implantation processes exert a significant control on the U-series budgets of detrital silicate grains. This process may play a significant role in other hyperarid saline systems that facilitate the growth and preservation of soluble cements, such as Martian soils, for which the MDVs are an analog (Gibson et al., 1983). Given the time-dependence of this radiometric process, sedimentary  $\alpha$ -recoil implantation may offer some chronometric potential in studies of pedogenic and regolith processes, so long as other authigenic processes are adequately accounted for.

Even at the low degrees of chemical alteration characteristic of the McMurdo Dry Valleys, the  $^{230}\text{Th}$ - $^{234}\text{U}$ - $^{238}\text{U}$  systematics of fine sediments are highly sensitive to the processes of chemical weathering and alteration. U-series isotopes show extensive chemical mixing of several sediments with an endmember characterized by a clay-like component of the Taylor-IV drift (Fig. 8). Its isotopic signature appears in clay fractions as well as detrital fractions (as separated by Stokes settling), implying either resilient adhesion to particles or in situ alteration of detrital silicate that is not removed by leaching methods. While we have referred to this endmember as a “clay”, we did not ascertain its mineralogy, although its insolubility in leaching reagents suggests a silicate composition. It may be composed of true clay minerals:  $<63\ \mu\text{m}$  sediments from Taylor Valley contain illite, kaolinite, smectite, vermiculite, and mixed layer clays (Marra et al., 2017). Another component may be an authigenic amorphous silicate phase such as those observed in Antarctic subglacial weathering products (Graly et al., 2020) and precipitate rocks (Piccione et al., 2022). Indeed, amorphous  $\text{SiO}_2$  saturation is found in Lake Bonney waters and may also occur in sediment porewaters supported by  $\text{H}_2\text{SiO}_4$ -rich shallow groundwaters (Lyons et al., 1998, 2021).

## 5. Conclusions

The U-series isotopes of glaciogenic silts from Taylor Valley reflect complex weathering histories, with a suite of chemical and physical fractionation processes occurring across various spatiotemporal regimes. Indeed our findings of interconnected physicochemical weathering challenge the discrete separation of mechanical and physical processes and, rather, support the notion of integrated mechanical and chemical “rock decay” (Hall et al., 2012). In the context of U-series systematics, we observe a notable contribution from  $\alpha$ -recoil implantation from high-U authigenic phases into lower-U detrital phases. Our results confirm that  $\alpha$ -recoil implantation is a significant component of the U-series budget in sedimentary and pedogenic systems, as it is in fresh and weathered volcanic rocks (Tanaka et al., 2015; Menozzi et al., 2016). The complex suite of physicochemical weathering processes we observe, potentially including mineralogic memory of pre-communition  $\alpha$ -recoil damage, obfuscate the  $\alpha$ -recoil ejection signatures that predicate comminution dating, undermining its applicability in this and other sedimentary systems.

Despite the complex and non-unique U-series systematics, we construct a coherent chronology through coupled isotopic and elemental data (Table 4). The oldest and highest elevation Taylor-IV deposits record a  $>1\ \text{Ma}$  history entombed in soil salts, consistent with the 1500–2700 ka depositional age (Wilch et al., 1993; Brook et al., 1993); Taylor-III drifts record weathering with intermittent water contact since at least 400 ka, consistent with the upperbound depositional age of 450 ka (Brook et al., 1993); and the englacial Taylor-I sediments reflect a  $<100\ \text{ka}$  weathering history, indicating comparatively recent comminution. Collectively, the trends in U-series systematics indicate Late Pleistocene — and perhaps Holocene — subglacial comminution beneath Taylor Glacier, challenging canonical models of landscape

evolution in Taylor Valley and implying a more geomorphologically dynamic Taylor Glacier over the Pleistocene than previously assumed.

$\text{U}$ -series isotopes are remarkably sensitive to physicochemical weathering processes in detrital sediments, and record a wider range of these sedimentary weathering processes than oft-used major element indices of chemical weathering and alteration. In the context of ancient hyperarid regimes at high elevations in Taylor Valley, Antarctica,  $\alpha$ -recoil implantation processes are a dominant process and MDV soils present a key environment to explore these systematics further. We propose these same implantation processes might dominate sedimentary U-series behavior on analogous arid planetary surfaces, such as Mars, and may even offer chronometric potential for regolith processes in terrestrial and extraterrestrial desert environments.

## CRediT authorship contribution statement

**Graham Harper Edwards:** Writing – review & editing, Writing – original draft, Visualization, Software, Methodology, Investigation, Formal analysis, Data curation. **Gavin G. Piccione:** Writing – review & editing, Methodology, Investigation, Formal analysis. **Terrence Blackburn:** Writing – review & editing, Supervision, Resources, Project administration, Methodology, Investigation, Funding acquisition, Conceptualization. **Slawek Tulaczyk:** Writing – review & editing, Supervision, Project administration, Methodology, Investigation, Funding acquisition, Conceptualization.

## Declaration of competing interest

The authors declare that they have no known competing financial interests or personal relationships that could have appeared to influence the work reported in this paper.

## Acknowledgments

Many thanks to Brian Dreyer for his essential input into method development. We are deeply indebted to the U.S. Antarctic Program and its support staff during the 2017–2018 field season for making sample collection possible. This study was funded under NSF Awards 1644171 (T.B., S.T.), 2042495 (T.B., S.T.), and 2102591 (G.H.E.), and the NSF graduate research fellowship (G.P.).

## Appendix. U-series isotopic data

See Fig. A.1 and Table A.1.

## Appendix B. Supplementary data

Supplementary material related to this article can be found online at <https://doi.org/10.1016/j.chemgeo.2024.122463>.

## Data availability

All data and code underlying this study are available in the main text, supplementary materials, the github repository <https://github.com/grahamedwards/ComminWeath.jl>, and the U.S. Antarctic Program Data Center <https://doi.org/10.15784/601806>.

Table A.1

U-Th isotopic data for Taylor Valley drift sediments. “Unit” refers to the Taylor Valley drift units Taylor I–IV, “D” refers to grain diameter, “Leach” refers to the number of complete sequential extraction cycles completed, and elemental concentrations (in  $\mu\text{g/g}$ ) are denoted with brackets. Uncertainty of  $[\text{U}]$  is closely approximated at  $2\sigma = 1.4\%$ , derived predominantly from uncertainty in tracer  $[^{236}\text{U}]$ . All other uncertainties are  $2\sigma$  absolute standard error and include tracer uncertainties. Parentheses indicate activity ratios calculated with decay constants from Cheng et al. (2013). All measurements including the isotope  $^{232}\text{Th}$  are reported without uncertainties, since anomalous shifts in Fara-Daly gain may result in inaccuracies in  $^{232}\text{Th}$  measurements (up to 20%) unaccounted for by the calculated uncertainties (Appendix Fig. A.1). Calculated  $2\sigma$  uncertainties are  $\sim 1.8\%$  for  $[\text{Th}]$  and range from 2–5% (mean of 2.1%) for  $^{232}\text{Th}/^{238}\text{U}$  and 1–10% (mean of 2.6%) for  $(^{230}\text{Th}/^{232}\text{Th})$ . A machine-readable (.csv) version of this table that includes analytical uncertainties of all isotope ratios is available in the Supplementary Material.

Fraction	Unit	D ( $\mu\text{m}$ )	Settling rate	Leach	$[\text{U}]$	$(^{234}\text{U}/^{238}\text{U})$	$2\sigma$	$(^{230}\text{Th}/^{238}\text{U})$	$2\sigma$	$(^{235}\text{U}/^{238}\text{U})$	$2\sigma$	$[\text{Th}]$	$(^{232}\text{Th}/^{238}\text{U})$	$(^{230}\text{Th}/^{232}\text{Th})$
TV-I-1RL-1	T-I	10–20	Rapid (detrital)	3	1.56	0.945	0.001	0.94	0.02	0.007251	1.0e-6	1.39	0.92	3.2
TV-I-2RL-1	T-I	20–38	Rapid (detrital)	3	0.23	0.956	0.003	0.99	0.02	0.007255	5.0e-6	0.343	1.5	2.0
TV-I-2RL-2	T-I	20–38	Rapid (detrital)	3	0.172	0.959	0.003	–	–	0.007274	7.0e-6	0.265	1.6	2.4
TV-I-2RL-3	T-I	20–38	Rapid (detrital)	3	0.174	0.955	0.003	–	–	0.007251	8.0e-6	0.277	1.6	3.2
TV-I-3RL-1	T-I	38–45	Rapid (detrital)	3	0.27	0.963	0.009	1.07	0.03	0.00729	3.1e-5	0.398	1.5	2.2
TV-I-3RL-2	T-I	38–45	Rapid (detrital)	5	0.209	0.954	0.004	1.03	0.04	0.00726	9.0e-6	0.294	1.4	2.2
TV-I-3RL-3	T-I	38–45	Rapid (detrital)	5	0.235	0.964	0.002	1.06	0.05	0.007256	5.0e-6	0.317	1.4	2.4
TV-I-4RL-1	T-I	75–125	Rapid (detrital)	5	0.19	0.952	0.017	1.0	0.03	0.007266	7.0e-6	0.406	2.2	1.4
TV-I-4RL-2	T-I	75–125	Rapid (detrital)	5	0.213	0.943	0.009	0.99	0.02	0.007248	6.0e-6	0.404	2.0	1.6
TV-I-1R-1	T-I	10–20	Rapid (detrital)	0	0.761	0.965	0.001	0.93	0.03	0.007257	1.0e-6	1.52	2.1	1.4
TV-I-2R-1	T-I	20–38	Rapid (detrital)	0	0.417	1.017	0.003	1.09	0.03	0.007254	4.0e-6	0.842	2.1	1.7
TV-I-4R-1	T-I	75–125	Rapid (detrital)	0	0.396	1.069	0.002	1.13	0.02	0.00725	4.0e-6	1.04	2.7	1.3
TV-I-S-1	T-I	<45	Slow (clay)	0	3.7	1.637	0.002	–	–	0.007255	4.0e-6	–	4.8	–
TV-I-SL-1	T-I	<45	Slow (clay)	5	0.267	1.091	0.002	–	–	0.007259	4.0e-6	–	2.2	–
TV-I-SL-2	T-I	<45	Slow (clay)	5	0.541	1.058	0.01	1.14	0.02	0.007242	7.0e-6	0.984	1.9	1.9
TV-II-2RL-1	T-II	20–38	Rapid (detrital)	3	0.538	1.048	0.004	1.05	0.02	0.007273	1.0e-5	0.451	0.86	3.8
TV-II-3RL-1	T-II	45–38	Rapid (detrital)	3	0.289	1.034	0.003	1.14	0.03	0.007252	6.0e-6	0.569	2.0	1.8
TV-II-3RL-2	T-II	45–38	Rapid (detrital)	3	0.277	1.04	0.003	1.11	0.03	0.007272	7.0e-6	0.555	2.1	1.7
TV-II-3RL-3	T-II	45–38	Rapid (detrital)	5	0.261	1.05	0.009	1.15	0.06	0.007258	4.7e-5	0.468	1.8	2.0
TV-II-4RL-1	T-II	90–125	Rapid (detrital)	5	0.187	0.997	0.005	1.23	0.04	0.007217	1.1e-5	0.439	2.4	1.6
TV-II-2R-1	T-II	20–38	Rapid (detrital)	0	1.57	1.093	0.001	0.94	0.02	0.007256	2.0e-6	2.89	1.9	1.6
TV-II-3R-1	T-II	45–38	Rapid (detrital)	0	0.577	1.011	0.001	1.08	0.08	0.007257	2.0e-6	3.83	6.8	0.5
TV-II-3R-2	T-II	45–38	Rapid (detrital)	0	0.536	1.009	0.002	1.34	0.05	0.007258	4.0e-6	2.96	5.7	0.74
TV-II-4R-1	T-II	90–125	Rapid (detrital)	0	0.361	1.0	0.003	1.16	0.05	0.007252	5.0e-6	1.75	5.0	0.74
TV-II-3S-1	T-II	45–38	Slow (clay)	0	2.84	1.208	0.004	–	–	0.007257	1.0e-5	–	–	–
TV-II-3S-1	T-II	45–38	Slow (clay)	5	0.233	0.985	0.012	1.07	0.02	0.007277	4.9e-5	0.393	1.7	1.9
TV-III-1RL-1	T-III	10–20	Rapid (detrital)	5	0.163	1.192	0.011	1.38	0.03	0.007238	5.0e-6	0.401	2.5	1.7
TV-III-1RL-2	T-III	10–20	Rapid (detrital)	5	0.161	1.201	0.006	1.37	0.03	0.007244	3.0e-6	0.401	2.6	1.7
TV-III-1RL-3	T-III	10–20	Rapid (detrital)	5	0.132	1.241	0.017	1.28	0.04	0.007255	8.0e-6	0.33	2.6	1.6
TV-III-2RL-1	T-III	20–38	Rapid (detrital)	5	0.183	1.114	0.034	1.19	0.03	0.007238	1.2e-5	0.464	2.6	1.4
TV-III-2RL-2	T-III	20–38	Rapid (detrital)	5	0.176	1.185	0.02	1.24	0.03	0.007296	1.2e-5	0.487	2.8	1.4
TV-III-2RL-3	T-III	20–38	Rapid (detrital)	5	0.178	1.178	0.014	1.22	0.03	0.007262	7.0e-6	0.528	3.0	1.3
TV-III-3RL-1	T-III	38–45	Rapid (detrital)	5	0.211	1.092	0.013	1.16	0.03	0.007256	9.0e-6	0.529	2.6	1.4
TV-III-3RL-2	T-III	38–45	Rapid (detrital)	5	0.208	1.074	0.03	1.12	0.03	0.007232	1.6e-5	0.514	2.5	1.4
TV-III-3RL-3	T-III	38–45	Rapid (detrital)	5	0.208	1.106	0.013	1.13	0.03	0.007248	1.0e-5	0.521	2.6	1.4
TV-III-4RL-1	T-III	75–125	Rapid (detrital)	5	0.303	1.003	0.003	1.02	0.02	0.007261	6.0e-6	0.801	2.7	1.2
TV-III-4RL-2	T-III	75–125	Rapid (detrital)	5	0.304	1.004	0.004	0.99	0.03	0.007244	1.1e-5	0.83	2.8	1.1
TV-III-4RL-3	T-III	75–125	Rapid (detrital)	5	0.276	0.99	0.015	1.03	0.02	0.007266	1.2e-5	0.722	2.7	1.2
TV-III-1R-1	T-III	10–20	Rapid (detrital)	0	0.59	1.03	0.002	1.12	0.03	0.007255	5.0e-6	3.63	6.3	0.56
TV-III-2R-1	T-III	20–38	Rapid (detrital)	0	0.499	1.005	0.007	1.1	0.03	0.00725	2.6e-5	2.93	6.0	0.57
TV-III-3R-1	T-III	45–38	Rapid (detrital)	0	0.803	1.025	0.003	1.05	0.03	0.007272	8.0e-6	4.53	5.8	0.57
TV-III-4R-1	T-III	75–125	Rapid (detrital)	0	0.572	0.986	0.002	0.99	0.05	0.007254	6.0e-6	2.6	4.7	0.67
TV-III-1SL-1	T-III	10–38	Slow (clay)	5	1.1	1.137	0.006	1.25	0.03	0.007239	4.0e-6	2.16	2.0	1.9
TV-III-2SL-1	T-III	45–38	Slow (clay)	5	1.07	1.141	0.009	1.23	0.03	0.007254	6.0e-6	2.2	2.1	1.8
TV-III-2S-1	T-III	45–38	Slow (clay)	0	4.27	1.101	0.002	1.12	0.09	0.007262	4.0e-6	19.6	4.7	0.75
TV-IV-R1L-1	T-IV	10–20	Rapid (detrital)	3	1.29	0.99	0.001	1.04	0.02	0.007259	1.0e-6	1.48	1.2	2.8
TV-IV-R1L-2	T-IV	10–20	Rapid (detrital)	5	1.35	0.988	0.004	1.01	0.02	0.007251	8.0e-6	1.14	0.87	3.6
TV-IV-R2L-1	T-IV	20–38	Rapid (detrital)	3	0.319	1.034	0.003	1.12	0.04	0.00725	8.0e-6	0.374	1.2	2.9
TV-IV-R2L-2	T-IV	20–38	Rapid (detrital)	3	0.337	1.044	0.003	1.13	0.03	0.007259	5.0e-6	0.445	1.4	2.6
TV-IV-R2L-3	T-IV	20–38	Rapid (detrital)	5	0.369	1.015	0.002	1.08	0.03	0.007254	4.0e-6	0.387	1.1	3.1
TV-IV-R3L-1	T-IV	38–45	Rapid (detrital)	3	0.141	1.113	0.002	1.26	0.05	0.00725	5.0e-6	0.23	1.7	2.4
TV-IV-R3L-2	T-IV	38–45	Rapid (detrital)	3	0.145	1.163	0.002	–	–	0.007257	3.0e-6	0.236	1.7	–
TV-IV-R3L-3	T-IV	38–45	Rapid (detrital)	5	0.112	1.087	0.007	1.19	0.05	0.007238	1.5e-5	0.143	1.3	2.9
TV-IV-R3L-4	T-IV	38–45	Rapid (detrital)	5	0.12	1.085	0.004	–	–	0.007253	9.0e-6	0.165	1.4	–
TV-IV-R3L-5	T-IV	38–45	Rapid (detrital)	5+EDTA	0.121	1.107	0.027	1.23	0.03	0.007255	1.3e-5	0.2	1.7	2.3
TV-IV-R4L-1	T-IV	75–125	Rapid (detrital)	5	0.177	1.006	0.005	0.98	0.04	0.00725	1.2e-5	0.293	1.7	1.8
TV-IV-R1-1	T-IV	10–20	Rapid (detrital)	0	1.76	1.057	0.001	1.39	0.03	0.007256	2.0e-6	12.6	7.4	0.6
TV-IV-R2-1	T-IV	20–38	Rapid (detrital)	0	0.872	1.05	0.007	1.1	0.03	0.007219	2.3e-5	5.83	6.9	0.51
TV-IV-R3-1	T-IV	38–45	Rapid (detrital)	0	0.453	1.09	0.005	1.28	0.03	0.007267	1.7e-5	2.83	6.4	0.63
TV-IV-R4-1	T-IV	75–125	Rapid (detrital)	0	0.418	1.004	0.003	1.15	0.03	0.007248	8.0e-6	2.03	5.0	0.72
TV-IV-S1L-1	T-IV	<38	Slow (clay)	5	0.689	1.234	0.002	1.48	0.03	0.007266	6.0e-6	1.2	1.8	2.6
TV-IV-S2L-1	T-IV	45–38	Slow (clay)	5	0.403	1.562	0.002	2.11	0.04	0.007258	3.0e-6	0.73	1.9	3.6
TV-IV-S2-1	T-IV	45–38	Slow (clay)	0	2.46	1.297	0.001	1.12	0.06	0.007251	2.0e-6	18.4	7.6	0.46
TV-IV-S2-2	T-IV	45–38	Slow (clay)	0	2.47	1.295	0.002	1.29	0.05	0.00725	2.0e-6	18.7	7.7	0.53
TV-IV-S2-1	T-IV	<38	Slow (clay)	0	2.64	1.245	0.002	1.25	0.04	0.007253	3.0e-6	19.4	7.5	0.52
TV-IV-S2-2	T-IV	<38	Slow (clay)	0	2.64	1.245	0.002	1.24	0.07	0.007253	2.0e-6	20.5	8.0	0.49

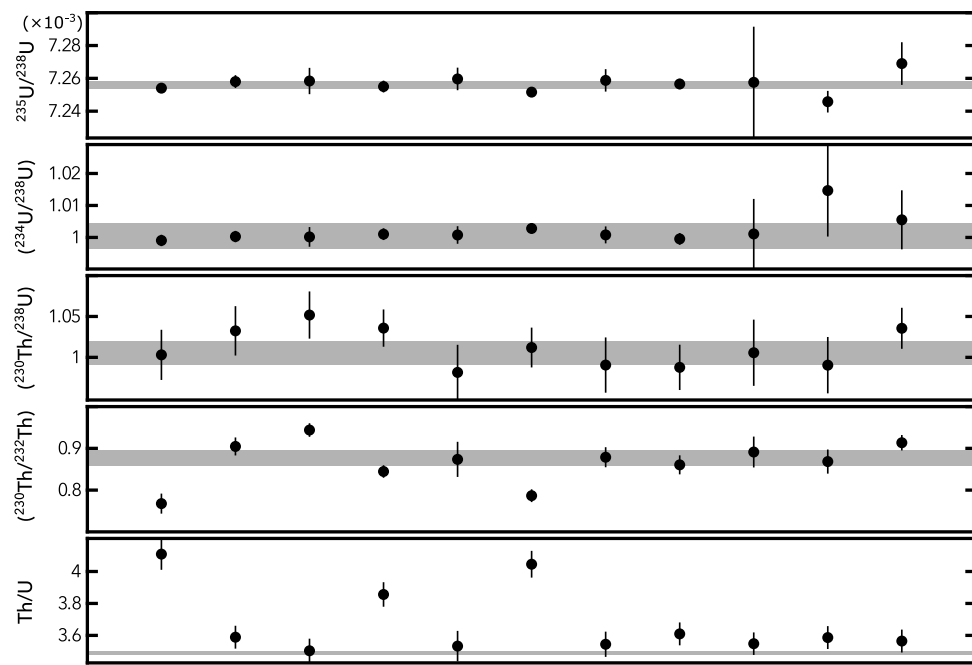


**Fig. A.1.** Measured U-Th isotope compositions of USGS rock standard BCR-2, compared to published values (gray bars; Koornneef et al., 2010).  $^{230}\text{Th}$ - $^{234}\text{U}$ - $^{238}\text{U}$  data consistently fall within the range of published compositions. All uncertainties are  $2\sigma$  standard error.

## References

Anbeek, C., Van Breemen, N., Meijer, E.L., Van Der Plas, L., 1994. The dissolution of naturally weathered feldspar and quartz. *Geochim. Cosmochim. Acta* 58 (21), 4601–4613. [http://dx.doi.org/10.1016/0016-7037\(94\)90194-5](http://dx.doi.org/10.1016/0016-7037(94)90194-5).

Andersen, M.B., Erel, Y., Bourdon, B., 2009. Experimental evidence for  $^{234}\text{U}$ - $^{238}\text{U}$  fractionation during granite weathering with implications for  $^{234}\text{U}$ - $^{238}\text{U}$  in natural waters. *Geochim. Cosmochim. Acta* <http://dx.doi.org/10.1016/j.gca.2009.04.020>.

Badgeley, J.A., Pettit, E.C., Carr, C.G., Tulaczyk, S., Mikucki, J.A., Lyons, W.B., 2017. An englacial hydrologic system of brine within a cold glacier: Blood falls, McMurdo Dry Valleys, Antarctica. *J. Glaciol.* 63 (239), 387–400. <http://dx.doi.org/10.1017/jog.2017.16>.

Bateman, H., 1910. Solution of a system of differential equations occurring in the theory of radioactive transformations. *Proc. Camb. Philos. Soc.* 15, 423–427.

Bezanson, J., Edelman, A., Karpinski, S., Shah, V.B., 2017. Julia: A fresh approach to numerical computing. *SIAM Rev.* 59 (1), 65–98. <http://dx.doi.org/10.1137/141000671>.

Blackburn, T., Edwards, G.H., Tulaczyk, S., Scudder, M., Piccione, G., Hallet, B., McLean, N., Zachos, J.C., Cheney, B., Babbe, J.T., 2020. Ice retreat in Wilkes Basin of East Antarctica during a warm interglacial. *Nature* 583 (7817), 554–559. <http://dx.doi.org/10.1038/s41586-020-2484-5>.

Blackburn, T., Siman-Tov, S., Coble, M.A., Stock, G.M., Brodsky, E.E., Hallet, B., 2019. Composition and formation age of amorphous silica coating glacially polished surfaces. *Geology* 47 (4), 347–350. <http://dx.doi.org/10.1130/G45737.1>.

Bockheim, J.G., 1997. Properties and classification of cold desert soils from Antarctica. *Soil Sci. Am. J.* 61 (1), 224–231. <http://dx.doi.org/10.2136/sssaj1997.03615995006100010031x>.

Bockheim, J.G., 2002. Landform and soil development in the McMurdo Dry Valleys, Antarctica: A regional synthesis. *Arct. Antarct. Alp. Res.* 34 (3), 308–317.

Bockheim, J.G., Prentice, M.L., McLeod, M., 2008. Distribution of glacial deposits, soils, and permafrost in Taylor Valley, Antarctica. *Arct. Antarct. Alp. Res.* 40 (2), 279–286. [http://dx.doi.org/10.1657/1523-0430\(06-057\)](http://dx.doi.org/10.1657/1523-0430(06-057).

Brook, E.J., Brown, E.T., Kurz, M.D., Ackert, R.P., Raisbeck, G.M., Yiou, F., 1995. Constraints on age, erosion, and uplift of neogene glacial deposits in the transantarctic mountains determined from *in situ* cosmogenic  $^{10}\text{Be}$  and  $^{26}\text{Al}$ . *Geology* 23 (12), 1063. [http://dx.doi.org/10.1130/0091-7613\(1995\)023<1063:COAEAU>2.3.CO;2](http://dx.doi.org/10.1130/0091-7613(1995)023<1063:COAEAU>2.3.CO;2).

Brook, E.J., Kurz, M.D., Ackert, R.P., Denton, G.H., Brown, E.T., Raisbeck, G.M., Yiou, F., 1993. Chronology of Taylor glacier advances in Arena Valley, Antarctica, using *in situ* cosmogenic  $^{3}\text{He}$  and  $^{10}\text{Be}$ . *Quat. Res.* 39 (1), 11–23. <http://dx.doi.org/10.1006/QRES.1993.1002>.

Campbell, I.B., Claridge, G.G.C., 1981. Soil research in the Ross Sea region of Antarctica. *J. R. Soc. N. Z.* 11 (4), 401–410. <http://dx.doi.org/10.1080/03036758.1981.10423330>.

Cartwright, J., 1962. Particle shape factors. *Ann. Occup. Hyg.* 5 (3), 163–171. <http://dx.doi.org/10.1093/annhyg/5.3.163>.

Chabaux, F., Blaes, E., Stille, P., di Chiara Roupert, R., Pelt, E., Dosseto, A., Ma, L., Buss, H.L., Brantley, S.L., 2013. Regolith formation rate from U-series nuclides: Implications from the study of a spheroidal weathering profile in the Rio Icacos watershed (Puerto Rico). *Geochim. Cosmochim. Acta* 100, 73–95. <http://dx.doi.org/10.1016/j.gca.2012.09.037>.

Chabaux, F., Riotti, J., Dequincey, O., 2003. U-Th-Ra fractionation during weathering and river transport. *Rev. Mineral. Geochem.* 52 (1), 533–576. <http://dx.doi.org/10.2113/0520533>.

Cheng, H., Edwards, R.L., Shen, C.C., Polyak, V.J., Asmerom, Y., Woodhead, J., Hellstrom, J., Wang, Y., Kong, X., Spötl, C., Wang, X., Alexander, E.C., 2013. Improvements in  $^{230}\text{Th}$  dating,  $^{230}\text{Th}$  and  $^{234}\text{U}$  half-life values, and U-Th isotopic measurements by multi-collector inductively coupled plasma mass spectrometry. *Earth Planet. Sci. Lett.* 371–372, 82–91. <http://dx.doi.org/10.1016/j.epsl.2013.04.006>.

Cogez, A., Herman, F., Pelt, É., Reuschlé, T., Morvan, G., Darvill, C.M., Norton, K.P., Christl, M., Märki, L., Chabaux, F., 2018. U-Th and  $^{10}\text{Be}$  constraints on sediment recycling in proglacial settings, Lago Buenos Aires, Patagonia. *Earth Surf. Dyn.* 6 (1), 121–140. <http://dx.doi.org/10.5194/esurf-6-121-2018>.

Cuffey, K.M., Conway, H., Gades, A.M., Hallet, B., Lorrain, R., Severinghaus, J.P., Steig, E.J., Vaughn, B., White, J.W., 2000. Entrainment at cold glacier beds. *Geology* 28 (4), 351–354. [http://dx.doi.org/10.1130/0091-7613\(2000\)028<0351:EACGB>2.3.CO;2](http://dx.doi.org/10.1130/0091-7613(2000)028<0351:EACGB>2.3.CO;2).

Cuffey, K.M., Conway, H., Hallet, B., Gades, A.M., Raymond, C.F., 1999. Interfacial water in polar glaciers and glacier sliding at  $-17^{\circ}\text{C}$ . *Geophys. Res. Lett.* 26 (6), 751–754. <http://dx.doi.org/10.1029/1999GL900096>.

Denton, G.H., Armstrong, R.L., Stuiver, M., 1970. Late cenozoic glaciation in Antarctica: The record in the McMurdo Sound region. *Antarct. J. United States* 5, 15–22.

Denton, G.H., Bockheim, J.G., Wilson, S.C., Stuiver, M., 1989. Late Wisconsin and early Holocene glacial history, inner Ross Embayment, Antarctica. *Quat. Res.* 31 (2), 151–182. [http://dx.doi.org/10.1016/0033-5894\(89\)90004-5](http://dx.doi.org/10.1016/0033-5894(89)90004-5).

Denton, G.H., Sugden, D.E., Marchant, D.R., Hall, B.L., Wilch, T.I., 1993. East Antarctic ice sheet sensitivity to Pliocene climatic change from a Dry Valleys perspective. *Geogr. Ann. Ser. A, Phys. Geogr.* 75 (4), 155. <http://dx.doi.org/10.2307/521200>.

DePaolo, D.J., Maher, K., Christensen, J.N., McManus, J., 2006. Sediment transport time measured with U-series isotopes: results from ODP North Atlantic drift site 984. *Earth Planet. Sci. Lett.* 248 (1–2), 379–395. <http://dx.doi.org/10.1016/j.epsl.2006.06.004>.

Deutsch, A.N., Levy, J.S., Dickson, J.L., Head, J.W., 2022. Daily and seasonal processes shape hydrological activity and detectability of moisture in Antarctic, Mars-analog soils. *Icarus* 114990. <http://dx.doi.org/10.1016/j.icarus.2022.114990>.

Diaz, M.A., Adams, B.J., Welch, K.A., Welch, S.A., Opiyo, S.O., Khan, A.L., McKnight, D.M., Cary, S.C., Lyons, W.B., 2018. Aeolian material transport and its role in landscape connectivity in the McMurdo Dry Valleys, Antarctica. *J. Geophys. Res.: Earth Surf.* 123 (12), 3323–3337. <http://dx.doi.org/10.1029/2017JF004589>.

Doran, P.T., McKay, C.P., Clow, G.D., Dana, G.L., Fountain, A.G., Nylen, T., Lyons, W.B., 2002. Valley floor climate observations from the McMurdo dry valleys, Antarctica,

1986–2000. *J. Geophys. Res.: Atmos.* 107 (24), 4772. <http://dx.doi.org/10.1029/2001JD002045>.

Dosseto, A., Buss, H.L., Suresh, P.O., 2012. Rapid regolith formation over volcanic bedrock and implications for landscape evolution. *Earth Planet. Sci. Lett.* 337–338, 47–55. <http://dx.doi.org/10.1016/j.epsl.2012.05.008>.

Dosseto, A., Schaller, M., 2016. The erosion response to quaternary climate change quantified using uranium isotopes and in situ-produced cosmogenic nuclides. *Earth-Sci. Rev.* 155, 60–81. <http://dx.doi.org/10.1016/j.earscirev.2016.01.015>.

Fitzpatrick, J.J., Muhs, D.R., Jull, A.J.T., 1990. Saline minerals in the lewis cliff ice tongue, buckley island quadrangle, antarctica. In: Contributions To Antarctic Research I. In: Antarctic Research Series, vol. 50, American Geophysical Union, pp. 57–69. <http://dx.doi.org/10.1029/ar050p0057>.

Fitzsimons, S., Samyn, D., Lorrain, R., 2024. Deformation, strength and tectonic evolution of basal ice in taylor glacier, Antarctica. *J. Geophys. Res.: Earth Surf.* 129 (4), e2023JF007456. <http://dx.doi.org/10.1029/2023JF007456>.

Fountain, A.G., Nylen, T.H., MacClune, K.L., Dana, G.L., 2006. Glacier mass balances (1993–2001), Taylor Valley, McMurdo Dry Valleys, Antarctica. *Journal of Glaciology* 52 (178), 451–462. <http://dx.doi.org/10.3189/172756506781828511>.

Gibson, E.K., Wentworth, S.J., McKay, D.S., 1983. Chemical weathering and diagenesis of a cold desert soil from Wright Valley, Antarctica: An analog of Martian weathering processes. *J. Geophys. Res.* 88, A912–A928. <http://dx.doi.org/10.1029/jb088is02p0912>.

Gillies, J.A., Nickling, W.G., Tilson, M., 2009. Ventifacts and wind-abraded rock features in the Taylor Valley, antarctica. *Geomorphology* 107 (3), 149–160. <http://dx.doi.org/10.1016/j.geomorph.2008.12.007>.

Goldberg, K., Humayun, M., 2010. The applicability of the chemical index of alteration as a paleoclimate indicator: An example from the Permian of the Paraná Basin, Brazil. *Palaeogeogr. Palaeoclimatol. Palaeoecol.* 293 (1–2), 175–183. <http://dx.doi.org/10.1016/j.palaeo.2010.05.015>.

Graly, J.A., Humphrey, N.F., Harper, J.T., 2016. Chemical depletion of sediment under the Greenland ice sheet. *Earth Surf. Process. Landf.* 41 (13), 1922–1936. <http://dx.doi.org/10.1002/esp.3960>.

Graly, J.A., Licht, K.J., Bader, N.A., Bish, D.L., 2020. Chemical weathering signatures from Mt. Achernar Moraine, Central Transantarctic Mountains I: Subglacial sediments compared with underlying rock. *Geochim. Cosmochim. Acta* 283, 149–166. <http://dx.doi.org/10.1016/j.gca.2020.06.005>.

Haldorsen, S., 1981. Grain-size distribution of subglacial till and its reaktion to glacial crushing and abrasion. *Boreas* 10 (1), 91–105. <http://dx.doi.org/10.1111/j.1502-3885.1981.tb00472.x>.

Hall, K., André, M.-F., 2001. New insights into rock weathering from high-frequency rock temperature data: An Antarctic study of weathering by thermal stress. *Geomorphology* 41 (1), 23–35. [http://dx.doi.org/10.1016/S0169-555X\(01\)00101-5](http://dx.doi.org/10.1016/S0169-555X(01)00101-5).

Hall, B.L., Denton, G.H., Henty, C.H., 2000. Evidence from Taylor Valley for a grounded ice sheet in the Ross Sea, Antarctica. *Geogr. Ann. Ser. A: Phys. Geogr.* 82 (2–3), 275–303. <http://dx.doi.org/10.1111/j.0435-3676.2000.00126.x>.

Hall, K., Guglielmin, M., Strini, A., 2008. Weathering of granite in Antarctica: I. Light penetration into rock and implications for rock weathering and endolithic communities. *Earth Surf. Process. Landf.* 33 (2), 295–307. <http://dx.doi.org/10.1002/esp.1618>.

Hall, K., Thorn, C., Sumner, P., 2012. On the persistence of ‘Weathering’. *Geomorphology* 149–150, 1–10. <http://dx.doi.org/10.1016/j.geomorph.2011.12.024>.

Hallet, B., Hunter, L., Bogen, J., 1996. Rates of erosion and sediment evacuation by glaciers: A review of field data and their implications. *Glob. Planet. Change* 12 (1–4), 213–235. [http://dx.doi.org/10.1016/0921-8181\(95\)00021-6](http://dx.doi.org/10.1016/0921-8181(95)00021-6).

Handley, H.K., Turner, S., Afonso, J.C., Dosseto, A., Cohen, T., 2013. Sediment residence times constrained by uranium-series isotopes: A critical appraisal of the comminution approach. *Geochim. Cosmochim. Acta* 103, 245–262. <http://dx.doi.org/10.1016/j.gca.2012.10.047>.

Henderson, G.M., Hall, B.L., Smith, A., Robinson, L.F., 2006. Control on  $^{234}\text{U}/^{238}\text{U}$  in lake water: A study in the dry valleys of Antarctica. *Chem. Geol.* 226 (3–4), 298–308. <http://dx.doi.org/10.1016/j.chemgeo.2005.09.026>.

Henty, C.H., Healy, T.R., Rayner, E.M., Shaw, J., Wilson, A.T., 1979. Late Pleistocene glacial chronology of the Taylor Valley, Antarctica, and the global climate. *Quat. Res.* 11 (2), 172–184. [http://dx.doi.org/10.1016/0033-5894\(79\)90002-4](http://dx.doi.org/10.1016/0033-5894(79)90002-4).

Higgins, S.M., Henty, C.H., Denton, G.H., 2000. Geochronology of Bonney Drift, Taylor Valley, Antarctica: Evidence for interglacial expansions of Taylor Glacier. *Geogr. Ann. Ser. A, Phys. Geogr.* 82 (2/3), 391–409. <http://dx.doi.org/10.1111/j.0435-3676.2000.00130.x>.

Hubbard, A., Lawson, W., Anderson, B., Hubbard, B., Blatter, H., 2004. Evidence for subglacial ponding across Taylor Glacier, Dry Valleys, Antarctica. *Ann. Glaciol.* 39, 79–84. <http://dx.doi.org/10.3189/172756404781813970>.

Jochum, K.P., Nohl, U., Herwig, K., Lammel, E., Stoll, B., Hofmann, A.W., 2005. GeoReM: A new geochemical database for reference materials and isotopic standards. *Geostand. Geoanal. Res.* 29 (3), 333–338. <http://dx.doi.org/10.1111/j.1751-908X.2005.tb00904.x>.

Kavanaugh, J.L., Cuffey, K.M., 2009. Dynamics and mass balance of Taylor Glacier, Antarctica: 2. Force balance and longitudinal coupling. *J. Geophys. Res.: Earth Surf.* 114 (4), F04011. <http://dx.doi.org/10.1029/2009JF001329>.

Kavanaugh, J.L., Cuffey, K.M., Morse, D.L., Conway, H., Rignot, E., 2009. Dynamics and mass balance of Taylor Glacier, Antarctica: 1. Geometry and surface velocities. *J. Geophys. Res.: Earth Surf.* 114 (4), <http://dx.doi.org/10.1029/2009JF001309>.

Kigoshi, K., 1971. Alpha-recoil Thorium-234: Dissolution into water and the Uranium-234/Uranium-238 disequilibrium in nature. *Science* 173 (3991), 47–48.

Knight, P.G., Waller, R.J., Patterson, C.J., Jones, A.P., Robinson, Z.P., 2002. Discharge of debris from ice at the margin of the Greenland ice sheet. *J. Glaciol.* 48 (161), 192–198.

Koornneef, J.M., Stracke, A., Aciego, S., Reubi, O., Bourdon, B., 2010. A new method for U-Th-Pa-Ra separation and accurate measurement of  $^{234}\text{U}$ - $^{230}\text{Th}$ - $^{231}\text{Pa}$ - $^{226}\text{Ra}$  disequilibria in volcanic rocks by MC-ICPMS. *Chem. Geol.* 277 (1–2), 30–41. <http://dx.doi.org/10.1016/j.chemgeo.2010.07.007>.

Ku, T.L., 1965. An evaluation of the  $^{234}\text{U}/^{238}\text{U}$  method as a tool for dating pelagic sediments. *J. Geophys. Res.* 70 (14), 3457–3474. <http://dx.doi.org/10.1029/JZ070i014p03457>.

Lee, V.E., DePaolo, D.J., Christensen, J.N., 2010. Uranium-series comminution ages of continental sediments: Case study of a Pleistocene alluvial fan. *Earth Planet. Sci. Lett.* 296 (3–4), 244–254. <http://dx.doi.org/10.1016/j.epsl.2010.05.005>.

Lyons, W.B., Leslie, D.L., Gooseff, M.N., 2021. Chemical weathering in the McMurdo Dry Valleys, Antarctica. In: Hydrogeology, Chemical Weathering, and Soil Formation. American Geophysical Union (AGU), pp. 205–216. <http://dx.doi.org/10.1002/9781119563952.ch11>.

Lyons, W.B., Welch, K.A., Neumann, K., Toxey, J.K., McArthur, R., Williams, C., McKnight, D.M., Moorhead, D.L., 1998. Geochemical linkages among glaciers, streams and lakes within the Taylor Valley, Antarctica. In: Ecosystem Dynamics in a Polar Desert; The McMurdo Dry Valleys, Antarctica, Vol. 72. American Geophysical Union (AGU), pp. 77–92. <http://dx.doi.org/10.1029/AR072p0077>.

MacGregor, K., Anderson, R., Anderson, S., Waddington, E., 2000. Numerical simulations of glacial-valley longitudinal profile evolution. *Geology* 28 (11), 1031–1034. [http://dx.doi.org/10.1130/0091-7613\(2000\)28<1031:NSOGLP>2.0.CO;2](http://dx.doi.org/10.1130/0091-7613(2000)28<1031:NSOGLP>2.0.CO;2).

Mager, S., Fitzsimons, S., Frew, R., 2007. Stable isotope composition of the basal ice from Taylor Glacier, Southern Victoria Land, Antarctica. In: 10th International Symposium on Antarctic Earth Sciences. pp. 1–4.

Marra, K.R., Elwood Madden, M.E., Soreghan, G.S., Hall, B.L., 2017. Chemical weathering trends in fine-grained ephemeral stream sediments of the McMurdo Dry Valleys, Antarctica. *Geomorphology* 281, 13–30. <http://dx.doi.org/10.1016/j.geomorph.2016.12.016>.

Martin, A.N., Dosseto, A., Kinsley, L.P., 2015. Evaluating the removal of non-detrital matter from soils and sediment using uranium isotopes. *Chem. Geol.* 396, 124–133. <http://dx.doi.org/10.1016/j.chemgeo.2014.12.016>.

Matsuoka, K., Skoglund, A., Roth, G., de Pomereu, J., Griffiths, H., Headland, R., Herried, B., Katsumata, K., Le Brocq, A., Licht, K., Morgan, F., Neff, P.D., Ritz, C., Scheinert, M., Tamura, T., Van de Putte, A., van den Broeke, M., von Deschwanden, A., Deschamps-Berger, C., Van Liefferinge, B., Tronstad, S., Melvær, Y., 2021. Quantarctica, an integrated mapping environment for Antarctica, the Southern Ocean, and sub-Antarctic islands. *Environ. Model. Softw.* 140, 105015. <http://dx.doi.org/10.1016/j.envsoft.2021.105015>.

Menozzi, D., Dosseto, A., Kinsley, L.P., 2016. Assessing the effect of sequential extraction on the uranium-series isotopic composition of a basaltic weathering profile. *Chem. Geol.* 446, 126–137. <http://dx.doi.org/10.1016/j.chemgeo.2016.05.031>.

Mikucki, J.A., Auken, E., Tulaczyk, S., Virginia, R.A., Schamper, C., Sørensen, K.I., Doran, P.T., Dugan, H., Foley, N., 2015. Deep groundwater and potential subsurface habitats beneath an Antarctic dry valley. *Nature Commun.* 6 (1), 6831. <http://dx.doi.org/10.1038/ncomms7831>.

Mikucki, J.A., Pearson, A., Johnston, D.T., Turchyn, A.V., Farquhar, J., Anbar, A.D., Schrag, D.P., Priscu, J.C., Lee, P.A., 2009. A contemporary microbially maintained subglacial ferrous “ocean”. *Science* 324 (5925), 397–400. <http://dx.doi.org/10.1126/science.1167350>.

Montross, S., Skidmore, M., Christner, B., Samyn, D., Tison, J.L., Lorrain, R., Doyle, S., Fitzsimons, S., 2014. Debris-rich basal ice as a microbial habitat, Taylor Glacier, Antarctica. *Geomicrobiol. J.* 31 (1), 76–81. <http://dx.doi.org/10.1080/01490451.2013.811316>.

Montross, S.N., Skidmore, M., Tranter, M., Kivimäki, A.L., Parkes, R.J., 2013. A microbial driver of chemical weathering in glaciated systems. *Geology* 41 (2), 215–218. <http://dx.doi.org/10.1130/G33572.1>.

Morgan, D., Putkonen, J., Balco, G., Stone, J., 2010. Quantifying regolith erosion rates with cosmogenic nuclides  $^{10}\text{Be}$  and  $^{26}\text{Al}$  in the McMurdo Dry Valleys, Antarctica. *J. Geophys. Res.: Earth Surf.* 115 (3), 1–17. <http://dx.doi.org/10.1029/2009JF001443>.

Nesbitt, H.W., Young, G.M., 1982. Early Proterozoic climates and plate motions inferred from major element chemistry of lutites. *Nature* 299 (5885), 715–717. <http://dx.doi.org/10.1038/299715a0>.

Obryk, M.K., Doran, P.T., Fountain, A.G., Myers, M., McKay, C.P., 2020. Climate from the McMurdo Dry Valleys, Antarctica, 1986–2017: Surface air temperature trends and redefined summer season. *J. Geophys. Res.: Atmos.* 125 (13), e2019JD032180. <http://dx.doi.org/10.1029/2019JD032180>.

Pettit, E.C., Whorton, E.N., Waddington, E.D., Sletten, R.S., 2014. Influence of debris-rich basal ice on flow of a polar glacier. *J. Glaciol.* 60 (223), 989–1006. <http://dx.doi.org/10.3189/2014JoG13J161>.

Piccione, G., Blackburn, T., Tulaczyk, S., Rasbury, E.T., Hain, M.P., Ibarra, D.E., Methner, K., Tinglof, C., Cheney, B., Northrup, P., Licht, K., 2022. Subglacial precipitates record Antarctic ice sheet response to late Pleistocene millennial climate cycles. *Nature Commun.* 13 (1), 5428. <http://dx.doi.org/10.1038/s41467-022-33009-1>.

Plater, A.J., Ivanovich, M., Dugdale, R.E., 1992. Uranium series disequilibrium in river sediments and waters: The significance of anomalous activity ratios. *Appl. Geochem.* 7 (2), 101–110. [http://dx.doi.org/10.1016/0883-2927\(92\)90029-3](http://dx.doi.org/10.1016/0883-2927(92)90029-3).

Poulton, S.W., Canfield, D.E., 2005. Development of a sequential extraction procedure for iron: Implications for iron partitioning in continental derived particulates. *Chem. Geol.* 214 (3–4), 209–221. <http://dx.doi.org/10.1016/j.chemgeo.2004.09.003>.

Rubin, K.H., 2001. Analysis of  $^{232}\text{Th}/^{230}\text{Th}$  in volcanic rocks: A comparison of thermal ionization mass spectrometry and other methodologies. *Chem. Geol.* 175 (3–4), 723–750. [http://dx.doi.org/10.1016/S0009-2541\(00\)00340-5](http://dx.doi.org/10.1016/S0009-2541(00)00340-5).

Semkow, T.M., 1991. Fractal model of radon emanation from solids. *Phys. Rev. Lett.* 66 (23), 3012–3015. <http://dx.doi.org/10.1103/PhysRevLett.66.3012>.

Shaw, S.E., 1962. Petrography of beacon sandstone samples from beacon height west, Upper Taylor Glacier, Antarctica. *N. Z. J. Geol. Geophys.* 5 (5), 733–739. <http://dx.doi.org/10.1080/00288306.1962.10417634>.

Spigel, R.H., Priscu, J.C., Obryk, M.K., Stone, W., Doran, P.T., 2018. The physical limnology of a permanently ice-covered and chemically stratified Antarctic lake using high resolution spatial data from an autonomous underwater vehicle. *Limnol. Oceanogr.* 63 (3), 1234–1252. <http://dx.doi.org/10.1002/lo.10768>.

Stern, T.A., Baxter, A.K., Barrett, P.J., 2005. Isostatic rebound due to glacial erosion within the Transantarctic Mountains. *Geology* 33 (3), 221–224. <http://dx.doi.org/10.1130/G21068.1>.

Sugden, D., Denton, G., 2004. Cenozoic landscape evolution of the convoy range to Mackay Glacier area, Transantarctic Mountains: Onshore to offshore synthesis. *Bull. Geol. Soc. Am.* 116 (7–8), 840–857. <http://dx.doi.org/10.1130/B25356.1>.

Sun, H., Semkow, T.M., 1998. Mobilization of thorium, radium and radon radionuclides in ground water by successive alpha-recoils. *J. Hydrol.* 205 (1–2), 126–136. [http://dx.doi.org/10.1016/S0022-1694\(97\)00154-6](http://dx.doi.org/10.1016/S0022-1694(97)00154-6).

Suresh, P.O., Dosseto, A., Handley, H.K., Hesse, P.P., 2014. Assessment of a sequential phase extraction procedure for uranium-series isotope analysis of soils and sediments. *Appl. Radiat. Isot.* 83, 47–55. <http://dx.doi.org/10.1016/j.apradiso.2013.10.013>.

Suresh, P., Dosseto, A., Hesse, P., Handley, H., 2013. Soil formation rates determined from uranium-series isotope disequilibria in soil profiles from the Southeastern Australian highlands. *Earth Planet. Sci. Lett.* 379, 26–37. <http://dx.doi.org/10.1016/j.epsl.2013.08.004>.

Tanaka, R., Yokoyama, T., Kitagawa, H., Tesfaye, D.B., Nakamura, E., 2015. Evaluation of the applicability of acid leaching for the  $^{238}\text{U}$ – $^{230}\text{Th}$  internal isochron method. *Chem. Geol.* 396, 255–264. <http://dx.doi.org/10.1016/j.chemgeo.2014.12.025>.

Tessier, A., Campbell, P.G., Bisson, M., 1979. Sequential extraction procedure for the speciation of particulate trace metals. *Anal. Chem.* 51 (7), 844–851. <http://dx.doi.org/10.1021/ac50043a017>.

Toner, J.D., Sletten, R.S., Prentice, M.L., 2013. Soluble salt accumulations in Taylor Valley, Antarctica: implications for paleolakes and Ross Sea ice sheet dynamics. *J. Geophys. Res.: Earth Surf.* 118 (1), 198–215. <http://dx.doi.org/10.1029/2012JF002467>.

Vermeesch, P., 2018. IsoplotR: A free and open toolbox for geochronology. *Geosci. Front.* 9 (5), 1479–1493. <http://dx.doi.org/10.1016/j.gsf.2018.04.001>.

White, A.F., Blum, A.E., Schulz, M.S., Bullen, T.D., Harden, J.W., Peterson, M.L., 1996. Chemical weathering rates of a soil chronosequence on granitic alluvium: I. Quantification of mineralogical and surface area changes and calculation of primary silicate reaction rates. *Geochim. Cosmochim. Acta* [http://dx.doi.org/10.1016/0016-7037\(96\)00106-8](http://dx.doi.org/10.1016/0016-7037(96)00106-8).

Wilch, T.L., Denton, G.H., Lux, D.R., McIntosh, W.C., 1993. Limited Pliocene glacier extent and surface uplift in Middle Taylor Valley, Antarctica. *Geogr. Ann. Ser. A, Phys. Geogr.* 75 (4), 331. <http://dx.doi.org/10.2307/521206>.